IMPLEMENTATION OF K-EPSILON TURBULENCE MODELS IN A TWO DIMENSIONAL PARALLEL NAVIER-STOKES SOLVER ON HYBRID GRIDS

A THESIS SUBMITTED TO
THE GRADUATE SCHOOL OF NATURAL AND APPLIED SCIENCES
OF
MIDDLE EAST TECHNICAL UNIVERSITY

BY

ONUR OZAN KALKAN

IN PARTIAL FULFILLMENT OF THE REQUIREMENTS
FOR
THE DEGREE OF MASTER OF SCIENCE
IN
AEROSPACE ENGINEERING

SEPTEMBER 2014

Approval of the thesis:

IMPLEMENTATION OF K-EPSILON TURBULENCE MODELS IN A TWO DIMENSIONAL PARALLEL NAVIER-STOKES SOLVER ON HYBRID GRIDS

submitted by **ONUR OZAN KALKAN** in partial fulfillment of the requirements for the degree of **Master of Science in Aerospace Engineering Department, Middle East Technical University** by,

Prof. Dr. Canan Özgen
Dean, Graduate School of **Natural and Applied Sciences** _____

Prof. Dr. Ozan Tekinalp
Head of Department, **Aerospace Engineering** _____

Prof. Dr. İsmail H. Tuncer
Supervisor, **Aerospace Engineering Dept., METU** _____

Examining Committee Members:

Assoc. Prof. Dr. Sinan EYİ
Aerospace Engineering Dept., METU _____

Prof. Dr. İsmail H. TUNCER
Aerospace Engineering Dept., METU _____

Assoc. Prof. Dr. Oğuz Uzol
Aerospace Engineering Dept., METU _____

Assoc. Prof. Dr. D. Funda Kurtuluş
Aerospace Engineering Dept., METU _____

Dr. Bora Kalpaklı
Roketsan Missiles Industries inc. _____

Date: 03.09.2014

I hereby declare that all information in this document has been obtained and presented in accordance with academic rules and ethical conduct. I also declare that, as required by these rules and conduct, I have fully cited and referenced all material and results that are not original to this work.

Name, Last name : Onur Ozan KALKAN

Signature :

ABSTRACT

IMPLEMENTATION OF K-EPSILON TURBULENCE MODELS IN A TWO DIMENSIONAL PARALLEL NAVIER-STOKES SOLVER ON HYBRID GRIDS

KALKAN, Onur Ozan

M. S., Department of Aerospace Engineering

Supervisor: Prof. Dr. İsmail H. TUNCER

September 2014, 82 pages

In this thesis, the popular k-ε turbulence model is implemented on a parallel, 2-dimensional, explicit, density-based, finite volume based Navier-Stokes solver works on hybrid grids, HYP2D. Among the other versions available in the open literature, standard version of the k-ε turbulence mode is studied. Launder-Spalding and Chieng-Launder wall functions are adapted to the turbulence model in order to investigate the effects of the strong gradients in the vicinity of the wall on the turbulence. In order to include the low-Reynolds-number effects near the wall Abid's and Abe-Kondoh-Nagano near wall models are also implemented. Flow over turbulent flat plate and RAE 2822 airfoil are studied for validation of the implementation. After the results show that the implementation is successful according to experimental data and other numerical solutions, NACA 0012 airfoil is simulated at different flow conditions and the effects of turbulence model on the results are discussed. The ability of simulating the turbulent flow with accuracy is acquired to HYP2D solver.

Key-words: Turbulence Modeling, k-ε Turbulence Model, Wall Functions, Turbulent Flows

ÖZ

K-EPSİLON TÜRBÜLANS MODELLERİNİN HİBRİT ÇÖZÜM AĞLARINDA İKİ BOYUTLU PARALEL NAVIER-STOKES ÇÖZÜCÜSÜNE EKLENMESİ

KALKAN, Onur Ozan
Yüksek Lisans, Havacılık ve Uzay Mühendisliği Bölümü
Tez Yöneticisi: Prof. Dr. İsmail H. TUNCER
Eylül 2014, 82 sayfa

Bu tez çalışmasında, popüler bir türbülans modeli olan k-ε türbülans modelinin paralel, 2-boyutlu, açık, yoğunluk tabanlı, sonlu hacimler temelli bir Navier-Stokes çözücüsüne (HYP2D) eklenmesi gerçekleştirilmiştir. Literatürde farklı versiyonları da bulunan k-ε türbülans modelinin standart versiyonu ile çalışılmıştır. Duvar kenarındaki çok yüksek değişimlerin türbülans üzerine etkilerini incelemek için Launder-Spalding ve Chieng-Launder duvar fonksiyonları modele adapte edilmiştir. Ayrıca, düşük Reynolds sayılarının duvar etrafındaki akışa etkilerinin incelenmesi için Abid ve Abe-Kondoh-Nagano duvar modelleri çözücüye eklenmiştir. Türbülanslı düz plaka ve RAE 2822 kanat profili üzerindeki akış için analizler yapılarak sonuçlar deneysel veriler ve daha önce doğrulanmış popüler bir akış çözücüsünden elde edilen sonuçlarla karşılaştırılarak doğrulanmıştır. Son olarak, NACA 0012 kanat kesitinin etrafındaki akış farklı akış koşulları için modellenmiş ve türbülans modellerinin sonuçlar üzerindeki etkileri ve türbülansın kanat etrafındaki akışa etkileri tartışılmıştır. Bu çalışma ile HYP2D çözücüsüne türbülanslı akışları da çözebilme yeteneği kazandırılmıştır.

Anahtar Kelimeler: Türbülans modelleme, k-ε Türbülans Modeli, Duvar Fonksiyonları, Türbülanslı Akış

To Deniz

ACKNOWLEDGMENT

I would like to express my deepest thanks and gratitude to Prof. Dr. İsmail H. TUNCER for his supervision, understanding, goodwill and great guidance.

I also would like to thank TÜBİTAK for supporting this study under the BİDEB-2211 program.

I specially would like to thank my wife Deniz BİKE KALKAN. She always encouraged me when I felt desperate about this study. I am very grateful for her great love, constant encouragement and endless support during this difficult period of my life.

I would like to thank my wonderful family who supported and encouraged me at every moment of my whole life.

TABLE OF CONTENTS

LIST OF TABLES

TABLES

LIST OF FIGURES

FIGURES

LIST OF SYMBOLS

a	speed of sound
B	empirical log-law constant ($=5$)
CFL	Courant-Friedrichs-Lewy number
$c_{1\varepsilon}$	turbulence model constant ($=1.44$)
$c_{2\varepsilon}$	turbulence model constant($=1.92$)
c_{μ}	turbulence model constant ($=0.09$)
c_{p}	specific heat of fluid at constant pressure
E	empirical log-law constant ($=9.793$)
e_T	total energy of fluid
ε	dissipation rate of turbulence kinetic energy
F	convective flux
$\overrightarrow{f_B}$	body forces
G	viscous flux
k	turbulence kinetic energy
K	thermal conductivity of fluid
K_l	laminar (molecular) thermal conductivity of fluid
K_t	turbulent thermal conductivity
κ	von Karman constant ($=0.41$)
L	characteristic length
M	Mach number
M_t	turbulent Mach number
ns	time level
p	fluid pressure
Pr	Prandtl number

Pr_t	turbulent Prandtl number
φ	any flow variable
Φ	source term of turbulence
Q	flow variables
δQ	spatial difference of flow variables
R	residual
Re	Reynolds number
$\vec{\dot{q}}$	heat transfer rate at the boundaries
S_{ij}	strain rate tensor
t	time
Δt	time step size
T	temperature of fluid
τ_w	wall shear stress
u	x-component of fluid velocity
u_τ	friction velocity
$\vec{V}$	velocity vector
v	y-component of fluid velocity
$\vec{\sigma}$	stress tensor
σ_k	turbulent Prandtl number for turbulence kinetic energy
σ_ε	turbulent Prandtl number for dissipation rate of turbulence kinetic energy
τ_{ij}	shear stress tensor
μ	fluid viscosity
μ_l	laminar (molecular) viscosity of fluid
μ_t	turbulent viscosity
δ_{ij}	Kronecker delta
γ	specific heat ratio
ρ	density

Ω	control volume
S	face of the control volume

Subscripts:

∞	free stream value
B	value at the boundary cell center
eff	effective
j	face value
L	left state value
$norm$	normal to face
P	value at the computational cell center
R	right state value
t	turbulent value
$tang$	tangent to face

Superscripts:

'	fluctuating value
*	non-dimensional value
ns	value at time step ns
+	non-dimensionalized values near the wall

CHAPTER 1

INTRODUCTION

Computational Fluid Dynamics (CFD) plays a key role in technological development of the industry. In particular, the design departments of the aerospace companies and institutes use CFD as an essential tool both for optimized flying structures and for routine applications. The rapid development of computer technology, in terms of accessibility of the ability to program any kind of application even on smart phones and the power that the processors have been gaining, provides the CFD community solving the most complex problems in fluid flow. Just remembering the words of Sir Horace Lamb at a meeting of British Association in London, 1932 [1], the most complex phenomenon in fluid dynamics can be realized: *"I am an old man now, and when I die and go to heaven there are two matters on which I hope for enlightenment. One is quantum electrodynamics, and the other is the turbulent motion of fluids. And about former I am rather optimistic."* Fortunately, the developing computer technology helps the scientists and engineers to understand the main properties of turbulent motion of fluids. In the very near future, people may find answers for the big questions about turbulence even they are alive.

The most of the flows are turbulent in aerospace applications. Therefore, efforts have been spent for many years in order to deal with the solution of turbulence which entirely affects the properties of flow. However, the models developed for approximating the physical properties and behaviors of turbulence have not achieved to be accepted by most of the fluid mechanics society. An ideal model development studies capturing the physics of the turbulence without much complexity are still conducted all over the world, even though some models are more popular.

This study is mainly focused on implementation of one of these popular turbulence model to a finite volume based CFD solver developed for 2D hybrid grids (Structured + unstructured), which is called HYP2D.

1.1 Characteristics of Turbulence

Turbulence is a word which cannot be defined properly in dictionary. Therefore, the pioneer of the turbulence research become an important guide for defining the term, turbulence. In 1937, G.I. Taylor and T. von Karman stated that [2]*"Turbulence is an irregular motion which in general makes its appearance in fluids, gaseous or liquid, when they flow past solid surfaces or even when neighboring streams of the same fluid flow past or over one another."*

Another definition of turbulence is made by Hinze [3]:*"Turbulent fluid motion is an irregular condition of flow in which the various quantities show a random variation with time and space coordinates, so that statistically distinct average values can be discerned."*

From these definitions the main characteristics of the turbulence can be derived as the randomness in time and space, irregularity and deterministic feature of average values. It can also be added that turbulence is essentially three dimensional because of the structures of the vortices which generate the turbulence. Another important characteristic of turbulence is that it is not a property of fluid but fluid flow [4].

1.2 Turbulence Modeling

Çıray [5] puts the reason of the need for modeling the turbulence as insufficient knowledge about it. Because of the inherently chaotic characteristic of turbulence, there is no unique or general model which approximates the essence of physics of turbulence. Indeed, it is seen that in order to find the Reynolds stresses by using Navier-Stokes equations one needs to solve infinite number of equations for infinite number of variables. Therefore, the only solution is to develop models specific to the flow problem

and considering the relevant flow variables. Many models have been developed with many specific assumptions related to the problem. However, most of them are usually not applicable when the flow properties or the assumptions change.

The main target of turbulence modeling is to model the Reynolds stresses. The first approach was the Boussinesq's model [6] proposed in 1877 in which the Reynolds stresses are defined by a relation similar to Newton's tangential (shear) stress equation. In this hypothesis, Boussinesq assumed that Reynolds stresses are governed by a turbulent viscosity or eddy viscosity which is supposed to be constant.

The second historical step to model Reynolds stresses are developed by G.I. Taylor [7] and L. Prandtl [8], separately, in 1915 and 1925, respectively. This model is called as mixing length model. In this approach, a physical model or a paradigm for the behavior of turbulence is assumed. Thus, this method is a phenomenological model. Mixing length model is a semi-empirical model for which a closure constant is determined by experiments and proper calibration.

The third important step is triggered by the development of CPUs. The "equation models" with too many variations are born to resolve to Reynolds stresses appearing in the Reynolds-Averaged Navier-Stokes Equations (RANS). Direct Numerical Simulation (DNS) for limited size of flow domain is performed for unsteady Navier-Stokes equations in order to realize the turbulence behavior. The weakness of all other models in predicting the large eddies are minimized with the help of Large Eddy Simulation (LES) model. This model is still more promising approach in order to solve turbulent flows with a relatively satisfactory precision.

1.2.1 Algebraic Models

Algebraic models are based on the mixing length model. Smagorinsky (1963) [9], Cebeci and Smith (1967) [10] and Baldwin and Lomax (1978) [11] proposed different approaches to the relationship between mixing length of turbulence and eddy viscosity.

Although Cebeci-Smith and Baldwin-Lomax models provide mixing length specifications that yield quite accurate results for attached boundary layer flows, the mixing length property is to be specified and heavily geometry-dependent.

1.2.2 One-Equation Models

One-Equation Models are called after the number of additional differential equations to be solved in order for modeling eddy viscosity. The first successful model is proposed by Bradshaw, Ferriss and Atwell (1967) [12]. After many years, some renewed interest in one-equation models have been shown by Baldwin and Barth(1990) [13] and Spalart and Allmaras(1992) [14]. Spalart-Allmaras model becomes very popular for the solution of turbulent flows in aerodynamics.

1.2.3 Two-Equation Models

The first two-equation model proposed by Kolmogorov (1942) [15] was the k-ω model, nevertheless it remained in obscurity until the use of computers. However, Launder, Jones and Spalding (1972) [16-17] made the most important contribution to the development of two-equation models, representing the k-ε model. This model is still the most popular turbulence model used in engineering application which is proved by an informal survey conducted over the ASME Journal of Fluids Engineering publications between 2009 and 2011 [18], see Figure 1.1. As it can be seen more than one half of these papers, different versions of the k-ε model are applied.

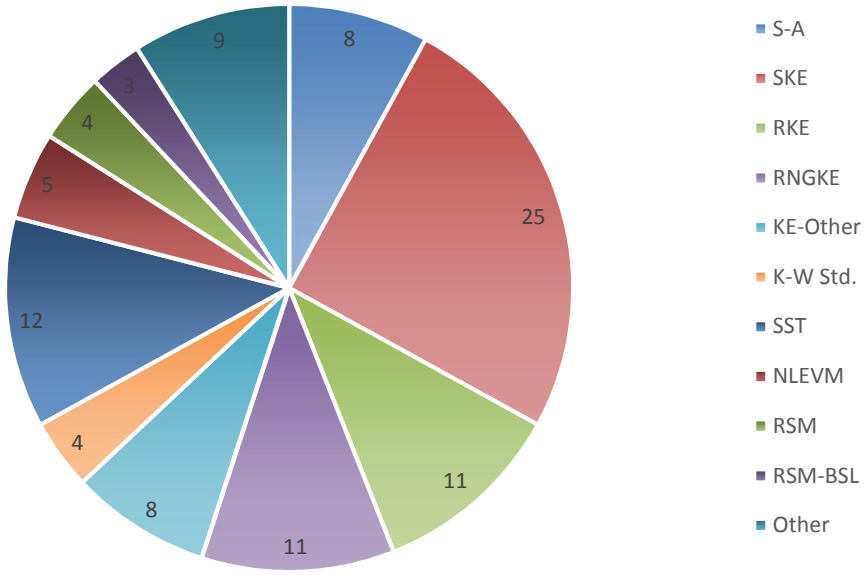

Figure 1.1. RANS Simulations Reported in ASME Journal of Fluids Engineering, 2009-2011 [18]

The efforts spent for k-ω model are also noteworthy. Wilcox [19] has contributed the further development of this model.

1.2.4 Large Eddy Simulation

Larger, three dimensional, unsteady turbulent motions which are geometry dependent, anisotropic and containing most of the energy are directly represented (computed explicitly), whereas the effects of smaller scale motions (which have more or less universal character) are modeled. There are four conceptual steps in Large Eddy Simulation (LES). The first is the filtering of Navier-Stokes equations in order to divide the properties into filtered (resolved) and sub-grid-scale (SGS) component. The second is the deriving the governing equations for the filtered component from Navier-Stokes

equations. Then SGS stress tensor is modeled to include the effect of small scale eddies. Finally, the filtered equations are solved.

1.2.5 Direct Numerical Simulation

In Direct Numerical Simulation (DNS), there is no need to model the turbulence since Navier-Stokes equations are solved numerically. Therefore, turbulence is directly solved for its whole range of time and length scales. In order to resolve even the smallest dissipative eddies (Kolmogorov scale) the computational grid should be adopted to be consisted of the length smaller than Kolmogorov scale. Therefore, DNS is still an expensive method for most of the flow problems.

1.3 Objective of the Thesis

The aim of this study is implementing a two-equation eddy viscosity turbulence model, k-ε model, to a parallel, two-dimensional, explicit, collocated finite volume solver for hybrid grids, HYP2D. Since, it is still the most popular model in turbulence community, k-ε turbulence model is preferred.

For the solution of the most critical phenomenon encountered in turbulent flows, near-wall effects, a numerically stable, computationally cheap and fast in convergence model is applied. So-called wall function approach avoids the very fine grid resolution near the wall region which makes this model attractive for engineering applications. In addition, two low-Reynolds-Numbers near-wall models (Abid [38] and Abe-Kondoh-Nagano [39]) are implemented for the comparison of wall functions and near-wall models.

The validation of the implementation is performed by comparing the results with the experiments and other numerical simulations.

CHAPTER 2

GOVERNING EQUATIONS

In this chapter, the general governing equations which describe the turbulent fluid motion are represented.

2.1 Conservation Equations

Laws of nature can be defined under three main laws: basic laws which are valid for systems and independent of substance and coordinate system, conservation laws, and subsidiary laws which are applicable only for a given substance and also particle dependent. There are mainly two ways of studying the laws of nature: following the system and control volume approach. The most common way, however, is transforming from system to the control volume by using Reynolds transport theorem [20]. The change in any property of the system with time can be expressed by the time rate of change of the property in a volume that the system has occupied at any time (control volume) and the net flux through the surface of this control volume at that time. Therefore, the conservation laws can be written for any control volume.

The conservation of mass for a control volume Ω, is described as follows:

$$\frac{\partial}{\partial t}\int_{\Omega}\rho d\Omega + \oint_{S}\rho\vec{V}\cdot\overrightarrow{dS} = 0 \tag{2.1.1}$$

where S is the surface of control volume Ω (control surface), ρ is density of fluid, $\vec{V}$ is the velocity of fluid and $\overrightarrow{dS}$ is an infinitesimal control surface vector.

Similarly, the conservation of linear momentum becomes:

$$\frac{\partial}{\partial t}\int_{\Omega}\rho\vec{V}d\Omega+\oint_{S}\rho\vec{V}\left(\vec{V}\cdot\overrightarrow{dS}\right)=\int_{\Omega}\overrightarrow{f_B}d\Omega+\oint_{S}\vec{\sigma}\cdot\overrightarrow{dS} \tag{2.1.2}$$

Here, $\overrightarrow{f_B}$ represents the body force acting on the control volume which is not only weight but also some forces in rotating systems, and $\vec{\sigma}$ is the stress tensor. The stress tensor for Newtonian fluids with Stokes assumption is expressed as follows:

$$\sigma_{ij}=-\left(p+\frac{2}{3}\mu\theta\right)\delta_{ij}+2\mu S_{ij} \tag{2.1.3}$$

where p is fluid pressure, μ is fluid viscosity, θ is the time rate of change of relative volumetric deformation and S_{ij} is the strain rate tensor which is defined as $0.5\left(\partial u_i/\partial x_j+\partial u_j/\partial x_i\right)$. In addition, δ_{ij} represents the Kronecker delta function which returns 1 while i and j is equal, 0 otherwise. The stress tensor can be divided in to two parts:

$$\sigma_{ij}=-p\delta_{ij}+\tau_{ij} \tag{2.1.4}$$

where τ_{ij} is deviatoric stress.

The third conservation law which is written for the total energy is such that:

$$\frac{\partial}{\partial t}\int_{\Omega}\rho e_T d\Omega+\oint_{S}\rho e_T\left(\vec{V}\cdot\overrightarrow{dS}\right)=\oint_{S}\vec{\dot{q}}\cdot\overrightarrow{dS}+\int_{\Omega}\rho\overrightarrow{f_B}\cdot\vec{V}d\Omega+\oint_{S}\left(\vec{\sigma}\cdot\vec{V}\right)\cdot\overrightarrow{dS} \tag{2.1.5}$$

where e_T indicates the total energy of fluid per unit mass, $\vec{\dot{q}}$ shows the heat transfer rate at the boundaries, which is also defined by the heat conductivity of fluid and temperature gradient such that $\vec{\dot{q}}=-k\nabla T$.

The derivations of the conservation laws and manipulations of these equations can be found in many fluid mechanics books such as [21], [22].

2.2 Reynolds-Averaged Navier-Stokes Equations

According to Reynolds [23] the instantaneous variables can be decomposed into mean and fluctuating parts.

$$\begin{aligned} \rho &= \overline{\rho} + \rho' \\ u &= \overline{u} + u' \\ v &= \overline{v} + v' \\ p &= \overline{p} + p' \\ T &= \overline{T} + T' \end{aligned} \tag{2.2.1}$$

Here, the bar top of the letters defines the mean value of this property and the apostrophe represents the fluctuation of this property from the mean value.

Substituting the decomposed variables into the conservation of mass and momentum equations and applying the properties of averaging operation with some manipulations, the Reynolds-Averaged Navier Stokes (RANS) equations can be easily obtained. RANS equations in derivative and Cartesian tensor form, neglecting the body forces, are such that:

$$\frac{\partial \rho}{\partial t} + \frac{\partial}{\partial x_i}\left(\rho u_i\right) = 0 \tag{2.2.2}$$

$$\frac{\partial}{\partial t}\left(\rho u_i\right) + \frac{\partial}{\partial x_j}\left(\rho u_i u_j\right) = -\frac{\partial p}{\partial x_i} + \frac{\partial}{\partial x_j}\left[\mu\left(\frac{\partial u_i}{\partial x_j} + \frac{\partial u_j}{\partial x_i} - \frac{2}{3}\delta_{ij}\frac{\partial u_k}{\partial x_k}\right)\right] + \frac{\partial}{\partial x_j}\left(-\rho\overline{u_i' u_j'}\right) \tag{2.2.3}$$

where, the mean properties are represented by dropping the bar sign. However, the last term in right hand side of Equation (2.2.3) appears as the mean of the correlation of velocity fluctuations which represents the effects of turbulence. The additional term $-\rho\overline{u_i' u_j'}$ is called the Reynolds stress tensor which is to be modeled. Wilcox [19] defines these additional terms as the fundamental problem of turbulence since the

symmetrical Reynolds stress tensor produces six unknowns without any additional equation which brings a closure problem to the equations system of turbulent flows. Therefore, turbulence modeling is indeed to model the Reynolds stresses appropriately to satisfy a closed-system.

Boussinesq [6] proposed the relation between the Reynolds stresses and the mean velocity gradients, which is commonly known as Boussinesq hypothesis:

$$-\rho\overline{u_i' u_j'} = \mu_t \left(\frac{\partial u_i}{\partial x_j} + \frac{\partial u_j}{\partial x_i} - \frac{2}{3}\frac{\partial u_k}{\partial x_k}\delta_{ij} \right) - \frac{2}{3}\rho k \delta_{ij} \tag{2.2.4}$$

where μ_t demonstrates the eddy viscosity or turbulent viscosity and k is the turbulence kinetic energy which is defined as:

$$k = \frac{1}{2}\overline{u_i' u_i'} \tag{2.2.5}$$

Applying the Boussinesq hypothesis to the RANS equations it is quite easy to close the equation system by modeling the turbulent viscosity.

2.3 k-ε Turbulence Model Equations

Although the first efforts trace to 1945s, works of Chou [24], the commonly accepted representation of k-ε turbulence model is developed by Jones and Launder [16] in 1972. In 1974, Launder and Sharma [25] and Launder and Spalding [26] represented the fine-tuned coefficients of the model and near wall effects on the model.

In order to model the turbulent viscosity, two transport equations are solved for turbulence kinetic energy, k, and turbulence dissipation rate, ε. Once this properties obtained the turbulent viscosity is calculated as a function of k and ε. The turbulent viscosity is related to this turbulent properties as follows:

$$\mu_t = f_\mu \rho c_\mu \frac{k^2}{\varepsilon} \tag{2.3.1}$$

where c_μ is the model constant while f_μ is damping function near the wall. The turbulent viscosity is assumed to be an isotropic scalar quantity. This assumption works well for many flow types, but, is not completely true.

The transport equation of k is derived from the exact Navier-Stokes equations, while the transport equation of ε is modeled since the exact equation for ε yields too many double and triple correlations of fluctuating properties which becomes nearly impossible to measure with any accuracy. Securing the physics of turbulence the transport equations for k and ε are presented such that:

$$\frac{\partial}{\partial t}(\rho k) + \underbrace{\frac{\partial}{\partial x_i}(\rho u_i k)}_{\text{Convection}_k} = \underbrace{\frac{\partial}{\partial x_j}\left[\left(\mu_l + \frac{\mu_t}{\sigma_k}\right)\frac{\partial k}{\partial x_j}\right]}_{\text{Diffusion}_k} + \text{Production}_k - \text{Destruction}_k - \text{Dilatation}_k \tag{2.3.2}$$

$$\frac{\partial}{\partial t}(\rho \varepsilon) + \underbrace{\frac{\partial}{\partial x_i}(\rho u_i \varepsilon)}_{\text{Convection}_\varepsilon} = \underbrace{\frac{\partial}{\partial x_j}\left[\left(\mu_l + \frac{\mu_t}{\sigma_\varepsilon}\right)\frac{\partial \varepsilon}{\partial x_j}\right]}_{\text{Diffusion}_\varepsilon} + \text{Production}_\varepsilon - \text{Destruction}_\varepsilon \tag{2.3.3}$$

where μ_l defines the laminar or molecular viscosity, σ_k and σ_ε are turbulent Prandtl numbers for k and ε, respectively. The terms in the transport equation of k are given below:

$$\text{Production}_k = -\rho \overline{u_i' u_j'} \frac{\partial u_j}{\partial x_i} \tag{2.3.4}$$

$$\text{Destruction}_k = \rho \varepsilon \tag{2.3.5}$$

$$\text{Dilatation}_k = 2\rho\varepsilon \text{M}_t^2 \tag{2.3.6}$$

where M_t is the turbulent Mach number defined as:

$$\mathrm{M}_t = \sqrt{\frac{k}{a^2}} \tag{2.3.7}$$

Here, a is speed of sound. The dissipation dilatation term is included only in compressible flows, in order to take into account of the effect of compressibility on the turbulent shear layers. This term is modeled according to Sarkar [27].

The terms in the transport equation of ε are as follows:

$$\text{Production}_\varepsilon = f_1 c_{1\varepsilon} \frac{\varepsilon}{k} \text{Production}_k \tag{2.3.8}$$

$$\text{Destruction}_\varepsilon = f_2 c_{2\varepsilon} \rho \frac{\varepsilon^2}{k} \tag{2.3.9}$$

where, $c_{1\varepsilon}$ and $c_{2\varepsilon}$ are the coefficients of the model, while f_1 and f_2 are the damping functions for the low-Reynolds-number models. The effect of buoyancy in turbulence kinetic energy production is neglected, so that production of turbulence kinetic energy is, only, due to velocity gradients.

The model constants suggested for the models studied in the context of this thesis are given in Table 2.1.

Table 2.1. k-ε Turbulence Model Coefficients

Model	$c_{1\varepsilon}$	$c_{2\varepsilon}$	σ_k	σ_ε	c_μ
Wall Function	1.44	1.92	1.0	1.3	0.09
Abid's Model	1.45	1.83	1.0	1.4	0.09
Abe-Kondoh-Nagano's Model	1.5	1.9	1.4	1.4	0.09

CHAPTER 3

SOLUTION ALGORITHM

In this chapter, the methodology to solve the governing equations of turbulent flow is proposed.

3.1 Non-dimensionalization

In order to reduce flow parameters to specific non-dimensional free parameters, such as Reynolds number, Mach number, Prandtl number, etc., the RANS equations and the turbulence model equations are non-dimensionalized using proper scales. The scales are as follows:

$$x^* = \frac{x}{L} \tag{3.1.1}$$

$$y^* = \frac{y}{L} \tag{3.1.2}$$

$$t^* = \frac{ta_\infty}{L} \tag{3.1.3}$$

$$u^* = \frac{u}{a_\infty} \tag{3.1.4}$$

$$v^* = \frac{v}{a_\infty} \tag{3.1.5}$$

$$\rho^* = \frac{\rho}{\rho_\infty} \tag{3.1.6}$$

$$p^* = \frac{p}{\rho_\infty a_\infty{}^2} \tag{3.1.7}$$

$$\mu_l^* = \frac{\mu_l}{\mu_\infty} \tag{3.1.8}$$

$$\mu_t^* = \frac{\mu_t}{\mu_\infty} \tag{3.1.9}$$

$$e_T{}^* = \frac{e_T}{a_\infty{}^2} \tag{3.1.10}$$

$$T^* = \frac{T}{T_\infty} \tag{3.1.11}$$

$$k^* = \frac{k}{a_\infty{}^2} \tag{3.1.12}$$

$$\varepsilon^* = \frac{\mu_\infty \varepsilon}{\rho_\infty a_\infty{}^4} \tag{3.1.13}$$

where, the subscript ∞ represents the free stream values and L is the characteristic length, for instance, chord length of airfoils or inner diameter of pipes.

The variables given in the RANS equations and k-ε turbulence model equations are replaced with the non-dimensionalized versions. Therefore, dropping the asterisk sign, the non-dimensional RANS equations for 2D turbulent flows are derived as follows:

$$\frac{\partial}{\partial t}(\rho) + \frac{\partial}{\partial x}(\rho u) + \frac{\partial}{\partial y}(\rho v) = 0 \tag{3.1.14}$$

$$\frac{\partial}{\partial t}(\rho u) + \frac{\partial}{\partial x}\left(\rho u^2 + p\right) + \frac{\partial}{\partial y}(\rho u v) = \frac{\mathrm{M}_\infty}{\mathrm{Re}_\infty}\frac{\partial}{\partial x}(\tau_{xx}) + \frac{\mathrm{M}_\infty}{\mathrm{Re}_\infty}\frac{\partial}{\partial y}(\tau_{xy}) \tag{3.1.15}$$

$$\frac{\partial}{\partial t}(\rho v)+\frac{\partial}{\partial x}(\rho uv)+\frac{\partial}{\partial y}\left(\rho v^2+p\right)=\frac{\mathrm{M}_\infty}{\mathrm{Re}_\infty}\frac{\partial}{\partial x}(\tau_{xy})+\frac{\mathrm{M}_\infty}{\mathrm{Re}_\infty}\frac{\partial}{\partial y}(\tau_{yy}) \tag{3.1.16}$$

$$\begin{aligned}&\frac{\partial}{\partial t}(\rho e_T)+\frac{\partial}{\partial x}(\rho e_T u+pu)+\frac{\partial}{\partial y}(\rho e_T v+pv)\\&=\frac{\mathrm{M}_\infty}{\mathrm{Re}_\infty}\frac{\partial}{\partial x}(u\tau_{xx}+v\tau_{xy})-\frac{1}{(\gamma-1)}\frac{1}{\mathrm{Pr}_\infty}\frac{\mathrm{M}_\infty}{\mathrm{Re}_\infty}\frac{\partial}{\partial x}(q_x)\\&+\frac{\mathrm{M}_\infty}{\mathrm{Re}_\infty}\frac{\partial}{\partial y}(u\tau_{xy}+v\tau_{yy})-\frac{1}{(\gamma-1)}\frac{1}{\mathrm{Pr}_\infty}\frac{\mathrm{M}_\infty}{\mathrm{Re}_\infty}\frac{\partial}{\partial y}(q_y)\end{aligned} \tag{3.1.17}$$

where the shear stresses τ_{ij} are defined as

$$\tau_{xx}=\underbrace{\frac{2}{3}\mu_l\left(2\frac{\partial u}{\partial x}-\frac{\partial v}{\partial y}\right)}_{\text{laminar}}+\underbrace{\frac{2}{3}\mu_t\left(2\frac{\partial u}{\partial x}-\frac{\partial v}{\partial y}\right)-2\rho k}_{\text{turbulent}} \tag{3.1.18}$$

$$\tau_{yy}=\underbrace{\frac{2}{3}\mu_l\left(2\frac{\partial v}{\partial y}-\frac{\partial u}{\partial x}\right)}_{\text{laminar}}+\underbrace{\frac{2}{3}\mu_t\left(2\frac{\partial v}{\partial y}-\frac{\partial u}{\partial x}\right)-2\rho k}_{\text{turbulent}} \tag{3.1.19}$$

$$\tau_{xy}=\tau_{yx}=\underbrace{\mu_l\left(\frac{\partial u}{\partial y}+\frac{\partial v}{\partial x}\right)}_{\text{laminar}}+\underbrace{\mu_t\left(\frac{\partial u}{\partial y}+\frac{\partial v}{\partial x}\right)}_{\text{turbulent}} \tag{3.1.20}$$

and the heat fluxes are as follows:

$$q_x=\underbrace{-k_l\frac{\partial T}{\partial x}}_{\text{laminar}}\underbrace{-k_t\frac{\partial T}{\partial x}-\frac{2}{3}\rho uk}_{\text{turbulent}} \tag{3.1.21}$$

$$q_y=\underbrace{-k_l\frac{\partial T}{\partial y}}_{\text{laminar}}\underbrace{-k_t\frac{\partial T}{\partial y}-\frac{2}{3}\rho vk}_{\text{turbulent}} \tag{3.1.22}$$

Here, turbulent thermal conductivity k_t can be found such that:

$$k_t = \frac{c_p \mu_t}{\mathrm{Pr}_t} \tag{3.1.23}$$

where c_p is the specific heat of fluid at constant pressure and Pr_t is the turbulent Prandtl number and has an average value of 0.85 for air.

k-ε turbulence model equations are also non-dimensionalized for convenience and given below:

$$\begin{aligned}
&\frac{\partial}{\partial t}(\rho k) + \frac{\partial}{\partial x}(\rho u k) + \frac{\partial}{\partial y}(\rho v k) \\
&= \frac{\mathrm{M}_\infty}{\mathrm{Re}_\infty}\frac{\partial}{\partial x}\left[\left(\mu_l + \frac{\mu_t}{\sigma_k}\right)\frac{\partial k}{\partial x}\right] + \frac{\mathrm{M}_\infty}{\mathrm{Re}_\infty}\frac{\partial}{\partial y}\left[\left(\mu_l + \frac{\mu_t}{\sigma_k}\right)\frac{\partial k}{\partial y}\right] \\
&+ \frac{\mathrm{M}_\infty}{\mathrm{Re}_\infty}\mathrm{Production}_k - \frac{\mathrm{Re}_\infty}{\mathrm{M}_\infty}\mathrm{Dissipation}_k - \frac{\mathrm{Re}_\infty}{\mathrm{M}_\infty}\mathrm{Dilatation}_k
\end{aligned} \tag{3.1.24}$$

$$\begin{aligned}
&\frac{\partial}{\partial t}(\rho \varepsilon) + \frac{\partial}{\partial x}(\rho u \varepsilon) + \frac{\partial}{\partial y}(\rho v \varepsilon) \\
&= \frac{\mathrm{M}_\infty}{\mathrm{Re}_\infty}\frac{\partial}{\partial x}\left[\left(\mu_l + \frac{\mu_t}{\sigma_\varepsilon}\right)\frac{\partial \varepsilon}{\partial x}\right] + \frac{\mathrm{M}_\infty}{\mathrm{Re}_\infty}\frac{\partial}{\partial y}\left[\left(\mu_l + \frac{\mu_t}{\sigma_\varepsilon}\right)\frac{\partial \varepsilon}{\partial y}\right] \\
&+ \frac{\mathrm{M}_\infty}{\mathrm{Re}_\infty}\mathrm{Production}_\varepsilon - \frac{\mathrm{Re}_\infty}{\mathrm{M}_\infty}\mathrm{Dissipation}_\varepsilon
\end{aligned} \tag{3.1.25}$$

Note that, all the variables are dimensionless, although the asterisk sign is not shown.

3.2 Discretization of RANS Equations

Non-dimensional RANS equations can be written as a linear system of equations:

$$\frac{\partial}{\partial t}\begin{bmatrix}\rho\\ \rho u\\ \rho v\\ \rho e_T\end{bmatrix}+\frac{\partial}{\partial x}\begin{bmatrix}\rho u\\ \rho u^2+p\\ \rho uv\\ \rho u e_T+pu\end{bmatrix}+\frac{\partial}{\partial y}\begin{bmatrix}\rho v\\ \rho uv\\ \rho v^2+p\\ \rho v e_T+pv\end{bmatrix}$$

$$=\frac{\partial}{\partial x}\begin{bmatrix}0\\ \frac{\mathrm{M}_\infty}{\mathrm{Re}_\infty}\tau_{xx}\\ \frac{\mathrm{M}_\infty}{\mathrm{Re}_\infty}\tau_{xy}\\ \frac{\mathrm{M}_\infty}{\mathrm{Re}_\infty}\left(u\tau_{xx}+v\tau_{xy}\right)-\frac{1}{(\gamma-1)}\frac{1}{\mathrm{Pr}_\infty}\frac{\mathrm{M}_\infty}{\mathrm{Re}_\infty}q_x\end{bmatrix}+\frac{\partial}{\partial y}\begin{bmatrix}0\\ \frac{\mathrm{M}_\infty}{\mathrm{Re}_\infty}\tau_{xy}\\ \frac{\mathrm{M}_\infty}{\mathrm{Re}_\infty}\tau_{yy}\\ \frac{\mathrm{M}_\infty}{\mathrm{Re}_\infty}\left(u\tau_{xy}+v\tau_{yy}\right)-\frac{1}{(\gamma-1)}\frac{1}{\mathrm{Pr}_\infty}\frac{\mathrm{M}_\infty}{\mathrm{Re}_\infty}q_y\end{bmatrix} \tag{3.2.1}$$

In Equation (3.2.1), the first term on the left hand side represents the conservative flow variables to be solved. The second and third terms on the left hand side are the x- and y-components of the convective flux of the conservative flow variables through the control volume faces. On the right hand side of the equation, the x- and y- components of the viscous and heat flux term are represented, respectively.

The new variables for the above linear system of equations are defined in a vector form as follows:

$$\vec{Q}=\begin{bmatrix}\rho\\ \rho u\\ \rho v\\ \rho e_T\end{bmatrix}: \text{Flow Variables Vector} \tag{3.2.2}$$

$$\overrightarrow{F_x}=\begin{bmatrix}\rho u\\ \rho u^2+p\\ \rho uv\\ \rho u e_T+pu\end{bmatrix}: \text{ Convective Flux Vector in x-direction} \tag{3.2.3}$$

$$\overrightarrow{F_y} = \begin{bmatrix} \rho v \\ \rho uv \\ \rho v^2 + p \\ \rho v e_T + pv \end{bmatrix} : \text{ Convective Flux Vector in y-direction} \qquad (3.2.4)$$

$$\overrightarrow{G_x} = \begin{bmatrix} 0 \\ \frac{\mathrm{M}_\infty}{\mathrm{Re}_\infty}\tau_{xx} \\ \frac{\mathrm{M}_\infty}{\mathrm{Re}_\infty}\tau_{xy} \\ \frac{\mathrm{M}_\infty}{\mathrm{Re}_\infty}\left(u\tau_{xx} + v\tau_{xy}\right) - \frac{1}{(\gamma-1)}\frac{1}{\mathrm{Pr}_\infty}\frac{\mathrm{M}_\infty}{\mathrm{Re}_\infty}q_x \end{bmatrix} : \text{ Viscous Flux Vector in x-direction} \quad (3.2.5)$$

$$\overrightarrow{G_y} = \begin{bmatrix} 0 \\ \frac{\mathrm{M}_\infty}{\mathrm{Re}_\infty}\tau_{xy} \\ \frac{\mathrm{M}_\infty}{\mathrm{Re}_\infty}\tau_{yy} \\ \frac{\mathrm{M}_\infty}{\mathrm{Re}_\infty}\left(u\tau_{xy} + v\tau_{yy}\right) - \frac{1}{(\gamma-1)}\frac{1}{\mathrm{Pr}_\infty}\frac{\mathrm{M}_\infty}{\mathrm{Re}_\infty}q_y \end{bmatrix} : \text{ Viscous Flux Vector in y-direction} \quad (3.2.6)$$

Equation (3.2.1) can now be simplified as

$$\frac{\partial}{\partial t}\vec{Q} + \frac{\partial}{\partial x}\overrightarrow{F_x} + \frac{\partial}{\partial y}\overrightarrow{F_y} = \frac{\partial}{\partial x}\overrightarrow{G_x} + \frac{\partial}{\partial y}\overrightarrow{G_y} \qquad (3.2.7)$$

The RANS equations can be integrated over the control volume Ω for which the boundary of it is defined as S, in vector form such as:

$$\frac{\partial}{\partial t}\int_\Omega \vec{Q}\,\mathrm{d}\Omega + \oint_S \vec{F}\cdot\overrightarrow{ds} = \oint_S \vec{G}\cdot\overrightarrow{ds} \qquad (3.2.8)$$

While performing the flux calculation, coordinate transformation is applied for the momentum equations. Instead of global x-y coordinate system, a local n-t coordinate system is defined. This local coordinate system is shown in Figure 3.1. In this figure, the red dotted axes which are labeled as n for the face normal direction and t for the face tangential direction are calculated for each cell face locally.

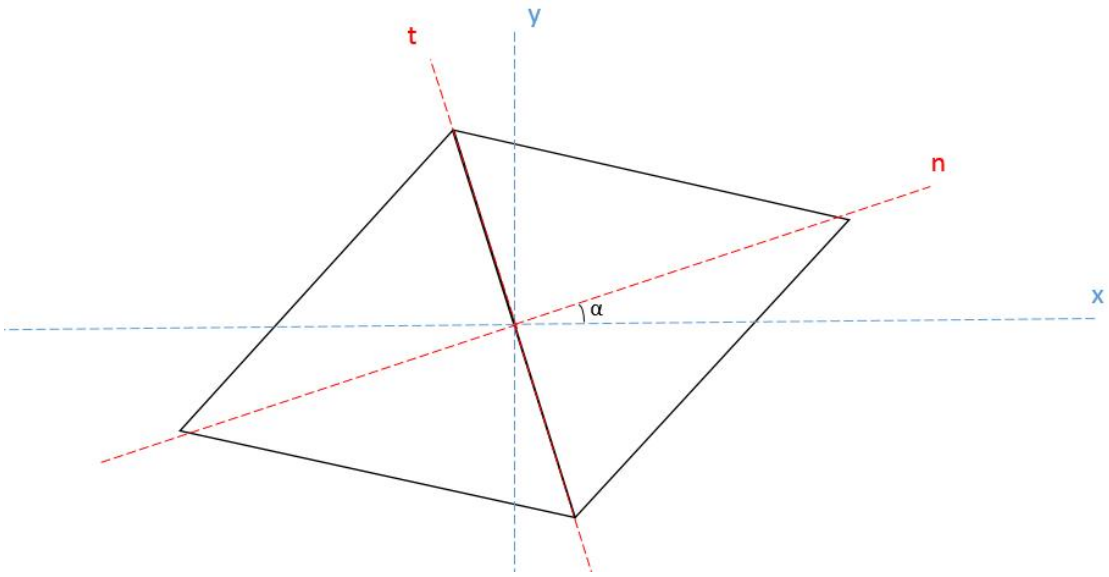

Figure 3.1. Coordinate Rotation for Flux Calculation

In this study, the momentum flux is assumed to be convected in the n-direction. Therefore, the momentum vectors are rotated to the normal direction of the surface using direction cosines while calculating the convective flux through the surface.

$$(\rho u)_{norm} = (\rho u)\cos(\alpha) + (\rho v)\sin(\alpha) \tag{3.2.9}$$

$$(\rho v)_{tang} = -(\rho u)\sin(\alpha) + (\rho v)\cos(\alpha) \tag{3.2.10}$$

After flux calculation, the terms including the momentum vector are rotated back to the x-y coordinate system as follows:

$$\rho u\vec{V} + p\vec{i} = \left(\left(\rho u \right)_{norm}{}^{2} + p \right) \cos(\alpha) - \left(\left(\rho u \right)_{norm} v_{tang} \right) \sin(\alpha) \tag{3.2.11}$$

$$\rho v\vec{V} + p\vec{j} = \left(\left(\rho u \right)_{norm}{}^{2} + p \right) \sin(\alpha) + \left(\left(\rho u \right)_{norm} v_{tang} \right) \cos(\alpha) \tag{3.2.12}$$

3.2.1 Discretization of Inviscid Fluxes

First, spatial discretization of the convective flux is proposed. The integral form of the RANS equations (see Equation(3.2.8)) will be used for this procedure. The convective flux term which is integrated over the control volume surface can be simply discretized by a second order numerical integration:

$$\oint_S \vec{F} \cdot \vec{ds} = \sum_{j=1}^{n_{face}} \vec{F_j} \cdot \vec{S_j} \tag{3.2.13}$$

In order to make the discretization clear, the surface vector is represented in Figure 3.2.

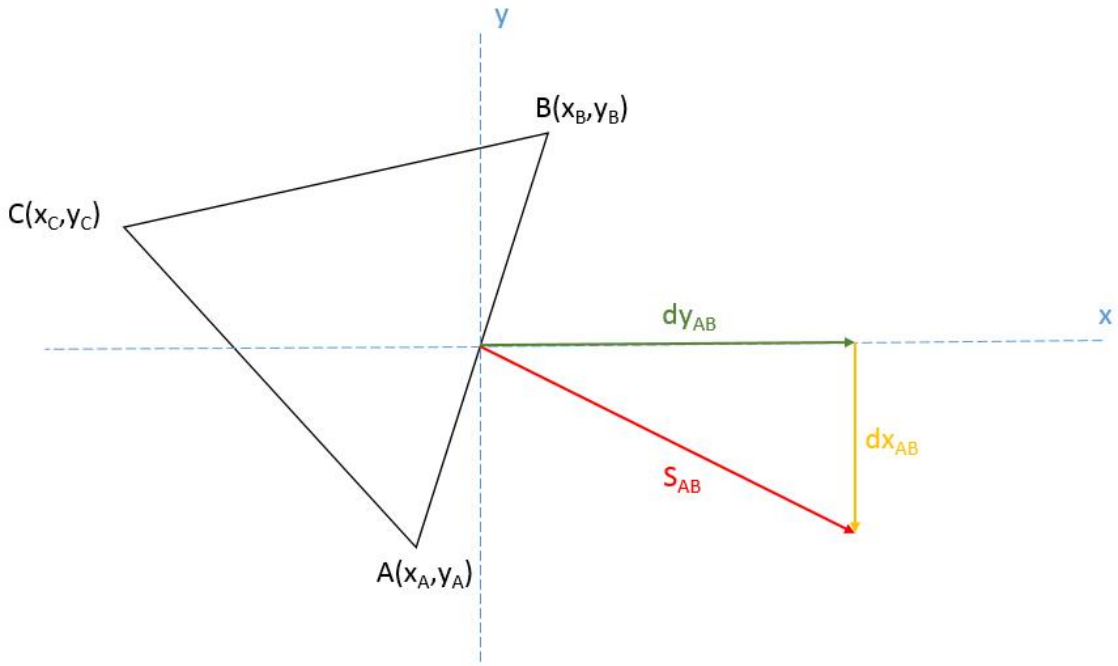

Figure 3.2. Components of Surface Vector in Cartesian Coordinate System

The surface vector of AB face of the control volume has the length of S_{AB}. This surface vector is defined using the cartesian coordinates of the nodes A and B.

$$\overrightarrow{S_{AB}} = \mathrm{dy}_{\mathrm{AB}}\vec{i} - \mathrm{dx}_{\mathrm{AB}}\vec{j} \tag{3.2.14}$$

where

$$\mathrm{dx}_{\mathrm{AB}} = x_B - x_A \tag{3.2.15}$$

$$\mathrm{dy}_{\mathrm{AB}} = y_B - y_A \tag{3.2.16}$$

The convective flux vector $\vec{F}$ can be decomposed to its Cartesian component.

$$\vec{F} = F_x\vec{i} + F_y\vec{j} \tag{3.2.17}$$

Multiplying flux vector (Equation(3.2.17)) and surface vector (Equation(3.2.14)) yields

$$\sum_{j=1}^{n_{face}} \overrightarrow{F_j} \cdot \overrightarrow{S_j} = \sum_{j=1}^{n_{face}} \left(F_x \mathrm{dy} - F_y \mathrm{dx} \right)_j \tag{3.2.18}$$

The same discretization procedure can be applied for the viscous flux term. Thus,

$$\sum_{j=1}^{n_{face}} \overrightarrow{G_j} \cdot \overrightarrow{S_j} = \sum_{j=1}^{n_{face}} \left(G_x \mathrm{dy} - G_y \mathrm{dx} \right)_j \tag{3.2.19}$$

The transient term is simply treated as follows:

$$\frac{\partial}{\partial t}\int_{\Omega} \vec{Q}\mathrm{d}\Omega = \Omega\frac{\partial Q}{\partial t} \tag{3.2.20}$$

The convective fluxes are calculated using Roe flux-difference splitting scheme [28].

3.2.2 Discretization of Viscous Fluxes

Combining the Equations(3.2.18), (3.2.19) and (3.2.20) the discretized finite volume form of the integral RANS equations for a cell becomes:

$$\Omega \frac{\partial Q}{\partial t} + \sum_{j=1}^{n_{face}} \left(F_x \mathrm{dy} - F_y \mathrm{dx} \right)_j = \sum_{j=1}^{n_{face}} \left(G_x \mathrm{dy} - G_y \mathrm{dx} \right)_j \tag{3.2.21}$$

$$\Omega \frac{\partial Q}{\partial t} + \sum_{j=1}^{n_{face}} \left[\left(F_x \text{-} G_x \right) \mathrm{dy} \text{-} \left(F_y \text{-} G_y \right) \mathrm{dx} \right]_j = 0 \tag{3.2.22}$$

For viscous flows, the gradients of velocity components, temperature and turbulent properties become important. The gradient of any variable φ, for a given cell is obtained based on the Green's divergence theorem:

$$\vec{\nabla}\varphi = \frac{1}{\Omega} \oint_S \varphi \vec{ds} \tag{3.2.23}$$

This gradient can be calculated numerically such that:

$$\vec{\nabla}\varphi = \frac{1}{\Omega} \sum_{j=1}^{n_{face}} \varphi_j \vec{S_j} = \frac{1}{\Omega} \sum_{j=1}^{n_{face}} \varphi_j \left(\mathrm{dy} \vec{i} - \mathrm{dx} \vec{j} \right) \tag{3.2.24}$$

where

$$\varphi_j = \frac{\varphi_L + \varphi_R}{2} \tag{3.2.25}$$

Note that the gradients are calculated at the cell center. The gradient of a variable, by definition, is as follows:

$$\vec{\nabla}\varphi = \frac{\partial \varphi}{\partial x}\vec{i} + \frac{\partial \varphi}{\partial y}\vec{j} \tag{3.2.26}$$

The gradients of the velocity components and temperature then become:

$$\vec{\nabla}u = \frac{\partial u}{\partial x}\vec{i} + \frac{\partial u}{\partial y}\vec{j} = \frac{1}{\Omega}\sum_{j=1}^{n_{face}} \frac{\left(u_L + u_R\right)_j}{2}\left(\mathrm{dy}\vec{i} - \mathrm{dx}\vec{j}\right) \tag{3.2.27}$$

$$\vec{\nabla}v = \frac{\partial v}{\partial x}\vec{i} + \frac{\partial v}{\partial y}\vec{j} = \frac{1}{\Omega}\sum_{j=1}^{n_{face}} \frac{\left(v_L + v_R\right)_j}{2}\left(\mathrm{dy}\vec{i} - \mathrm{dx}\vec{j}\right) \tag{3.2.28}$$

$$\vec{\nabla}T = \frac{\partial T}{\partial x}\vec{i} + \frac{\partial T}{\partial y}\vec{j} = \frac{1}{\Omega}\sum_{j=1}^{n_{face}} \frac{\gamma\left(\frac{p_L}{\rho_L} + \frac{p_R}{\rho_R}\right)_j}{2}\left(\mathrm{dy}\vec{i} - \mathrm{dx}\vec{j}\right) \tag{3.2.29}$$

While calculating the viscous fluxes, it is necessary to compute the gradients of velocity components and temperature at the faces of the control volumes. The initial approach for calculation of face gradients is just simply averaging the gradients of the cells which share the related face. However, this may result to oscillatory solutions [32]. In order to avoid the oscillations and take into account of the non-orthogonality of the grid structure, the face gradient of dummy variable φ, is calculated as follows:

$$\vec{\nabla}\varphi_{ij} = \overline{\vec{\nabla}\varphi_{ij}} + \left(\frac{\varphi_j - \varphi_i}{\left|\vec{r_j} - \vec{r_i}\right|} - \overline{\vec{\nabla}\varphi_{ij}} \cdot \hat{r}_{ij}\right)\hat{r}_{ij} \tag{3.2.30}$$

Here, the average of cell center gradients, $\overline{\vec{\nabla}\varphi_{ij}}$ which is defined such that

$$\overline{\vec{\nabla}\varphi_{ij}} = \frac{1}{2}\left(\vec{\nabla}\varphi_i + \vec{\nabla}\varphi_j\right) \tag{3.2.31}$$

is summed by the cross diffusion component and simple average of cell center values of the two adjacent cells. In addition, the unit vector $\hat{r}_{ij}$ from cell i to cell j is represented as follows where $\vec{r}_i$ and $\vec{r}_j$ are the state vectors of the two cell centers.

$$\hat{r}_{ij} = \frac{\vec{r}_j - \vec{r}_i}{\left|\vec{r}_j - \vec{r}_i\right|} \tag{3.2.32}$$

Then, using these face gradient values viscous stresses and the heat flux vector components at the faces are computed according to the Equations (3.1.18), (3.1.19), (3.1.20), (3.1.21) and (3.1.22).

Using Equations (3.2.5), (3.2.6) and (3.2.19), the viscous flux is computed and then subtracted from the convective flux to satisfy the Equation (3.2.22).

$$\overrightarrow{G_j}\cdot\overrightarrow{S_j} = \begin{bmatrix} 0 \\ \dfrac{\mathrm{M}_\infty}{\mathrm{Re}_\infty}\tau_{xx_j}\mathrm{dy}_j - \dfrac{\mathrm{M}_\infty}{\mathrm{Re}_\infty}\tau_{xy_j}\mathrm{dx}_j \\ \dfrac{\mathrm{M}_\infty}{\mathrm{Re}_\infty}\tau_{xy_j}\mathrm{dy}_j - \dfrac{\mathrm{M}_\infty}{\mathrm{Re}_\infty}\tau_{yy_j}\mathrm{dx}_j \\ G_E \end{bmatrix} \tag{3.2.33}$$

where

$$\begin{aligned} G_E = {} & \frac{\mathrm{M}_\infty}{\mathrm{Re}_\infty}\left(u_j\tau_{xx_j} + v_j\tau_{xy_j}\right)\mathrm{dy}_j - \frac{1}{(\gamma-1)}\frac{1}{\mathrm{Pr}_\infty}\frac{\mathrm{M}_\infty}{\mathrm{Re}_\infty}q_{x_j}\mathrm{dy}_j \\ & - \frac{\mathrm{M}_\infty}{\mathrm{Re}_\infty}\left(u_j\tau_{xy_j} + v_j\tau_{yy_j}\right)\mathrm{dx}_j + \frac{1}{(\gamma-1)}\frac{1}{\mathrm{Pr}_\infty}\frac{\mathrm{M}_\infty}{\mathrm{Re}_\infty}q_{y_j}\mathrm{dx}_j \end{aligned} \tag{3.2.34}$$

Here, the subscript j shows that the value is calculated at the related j^{th} face of the cell.

3.2.3 Temporal Discretization

After the flux calculations, temporal discretization is performed depending on the method preferred, implicit or explicit. In this study an explicit 3-step Runge-Kutta formulation is applied. For the n^{th} cell,

$$\Omega_n \frac{\partial Q_n}{\partial t} + \underbrace{\sum_{j=1}^{n_{face}} \left[\left(\vec{F_n} - \vec{G_n} \right) \cdot \vec{S_n} \right]_j}_{\text{Residual}=R_n} = 0 \tag{3.2.35}$$

$$\Omega_n \frac{\partial Q_n}{\partial t} + R_n = 0 \tag{3.2.36}$$

If the equations are discretized at the lime level *ns*, forward time differencing is employed for the time derivatives.

$$\Omega_n \frac{Q_n^{ns+1} - Q_n^{ns}}{\Delta t} + R_n^{ns} = 0 \tag{3.2.37}$$

Therefore, an explicit solution method is given as follows:

$$Q_n^{ns+1} = Q_n^{ns} - \frac{\Delta t}{\Omega_n} R_n^{ns} \tag{3.2.38}$$

For 3-stage Runge-Kutta method, the solution becomes

$$Q_n^{ns+1(0)} = Q_n^{ns} \tag{3.2.39}$$

$$Q_n^{ns+1(1)} = Q_n^{ns} - \alpha_1 \frac{\Delta t}{\Omega_n} R_n^{ns} (Q_n^{ns+1(0)}) \tag{3.2.40}$$

$$Q_n^{ns+1(2)} = Q_n^{ns} - \alpha_2 \frac{\Delta t}{\Omega_n} R_n^{ns} (Q_n^{ns+1(1)}) \tag{3.2.41}$$

$$Q_n^{ns+1(3)} = Q_n^{ns} - \alpha_3 \frac{\Delta t}{\Omega_n} R_n^{ns}(Q_n^{ns+1(2)}) \tag{3.2.42}$$

where

$$\begin{aligned} \alpha_1 &= \frac{1}{3} \\ \alpha_2 &= \frac{1}{2} \\ \alpha_3 &= 1 \end{aligned} \tag{3.2.43}$$

In order to obtain a faster steady state solution, a local time stepping scheme [33] is applied. The maximum allowable time step is calculated by two parts. The inviscid time step

$$\Delta t_i = \frac{\Delta L}{\sigma_{\max}} \tag{3.2.44}$$

and viscous time step

$$\Delta t_v = \frac{\rho(\Delta L)^2}{\mu + \mu_t} \tag{3.2.45}$$

are combined to obtain a final time step size for a stable solution with CFL number is less than 1 such that

$$\Delta t = CFL \frac{\Delta t_i \Delta t_v}{\Delta t_i + \Delta t_v} \tag{3.2.46}$$

Here, the maximum characteristic variable $\sigma_{\max}$ and characteristic length scale ΔL are calculated as follows:

$$\sigma_{\max} = \max \begin{Bmatrix} u+a \\ u-a \\ u \end{Bmatrix} \tag{3.2.47}$$

$$\Delta L_n = \frac{\Omega_n}{\max(S_j)} \tag{3.2.48}$$

3.3 Discretization of k-ε Turbulence Model Equations

k-ε turbulence model equations are calculated separate from the RANS equations. This segregated approach brings the disadvantage of computational effort spent for the calculation of a new equation system. On the other hand, it is more flexible to work with a segregated turbulence model approach.

Non-dimensional form of turbulence equations can be written as a linear system of equations.

$$\begin{aligned}
&\frac{\partial}{\partial t}\begin{bmatrix} \rho k \\ \rho \varepsilon \end{bmatrix} + \frac{\partial}{\partial x}\begin{bmatrix} \rho u k \\ \rho u \varepsilon \end{bmatrix} + \frac{\partial}{\partial y}\begin{bmatrix} \rho v k \\ \rho v \varepsilon \end{bmatrix} \\
&= \frac{\partial}{\partial x}\begin{bmatrix} \dfrac{\mathrm{M}_\infty}{\mathrm{Re}_\infty}\left(\mu_l + \dfrac{\mu_t}{\sigma_k}\right)\dfrac{\partial k}{\partial x} \\ \dfrac{\mathrm{M}_\infty}{\mathrm{Re}_\infty}\left(\mu_l + \dfrac{\mu_t}{\sigma_\varepsilon}\right)\dfrac{\partial \varepsilon}{\partial x} \end{bmatrix} + \frac{\partial}{\partial y}\begin{bmatrix} \dfrac{\mathrm{M}_\infty}{\mathrm{Re}_\infty}\left(\mu_l + \dfrac{\mu_t}{\sigma_k}\right)\dfrac{\partial k}{\partial y} \\ \dfrac{\mathrm{M}_\infty}{\mathrm{Re}_\infty}\left(\mu_l + \dfrac{\mu_t}{\sigma_\varepsilon}\right)\dfrac{\partial \varepsilon}{\partial y} \end{bmatrix} \\
&+ \frac{\mathrm{M}_\infty}{\mathrm{Re}_\infty}\begin{bmatrix} \mathrm{Production_k} \\ \mathrm{Production_\varepsilon} \end{bmatrix} - \frac{\mathrm{Re}_\infty}{\mathrm{M}_\infty}\begin{bmatrix} \mathrm{Destruction_k} \\ \mathrm{Destruction_\varepsilon} \end{bmatrix} - \frac{\mathrm{Re}_\infty}{\mathrm{M}_\infty}\begin{bmatrix} \mathrm{Dilatation_k} \\ 0 \end{bmatrix}
\end{aligned} \tag{3.3.1}$$

Integrating Equation (3.3.1) over the control volume and applying the same numerical integration used for RANS equations turbulence model equations are discretized as follows:

$$\Omega \frac{\partial Q_t}{\partial t} + \sum_{j=1}^{n_{face}} \left[\overrightarrow{F_{t_j}} \cdot \overrightarrow{S_j} - \overrightarrow{G_{t_j}} \cdot \overrightarrow{S_j} \mathrm{dx} \right]_j - \Omega\Phi_1 + \Omega\Phi_2 + \Omega\Phi_3 = 0 \tag{3.3.2}$$

where $\overrightarrow{F_t}$ stands for turbulent convective flux and similarly $\overrightarrow{G_t}$ is the turbulent diffusive flux. Terms represented by Φ are the source terms which are appearing in the k-ε turbulence model equations. The definitions of these properties are presented in vector form:

$$Q_t = \begin{bmatrix} \rho k \\ \rho \varepsilon \end{bmatrix} \tag{3.3.3}$$

$$\overrightarrow{F_{t_j}} \cdot \overrightarrow{S_j} = \begin{bmatrix} (\rho u k)_j \, dy_j - (\rho v k)_j \, dx_j \\ (\rho u \varepsilon)_j \, dy_j - (\rho v \varepsilon)_j \, dx_j \end{bmatrix} \tag{3.3.4}$$

$$\overrightarrow{G_{t_j}} \cdot \overrightarrow{S_j} = \begin{bmatrix} \dfrac{\mathrm{M}_\infty}{\mathrm{Re}_\infty}\left(\mu_l + \dfrac{\mu_{t_j}}{\sigma_k}\right)\left(\dfrac{\partial k}{\partial x}\right)_j dy_j - \dfrac{\mathrm{M}_\infty}{\mathrm{Re}_\infty}\left(\mu_l + \dfrac{\mu_{t_j}}{\sigma_k}\right)\left(\dfrac{\partial k}{\partial y}\right)_j dx_j \\ \dfrac{\mathrm{M}_\infty}{\mathrm{Re}_\infty}\left(\mu_l + \dfrac{\mu_{t_j}}{\sigma_\varepsilon}\right)\left(\dfrac{\partial \varepsilon}{\partial x}\right)_j dy_j - \dfrac{\mathrm{M}_\infty}{\mathrm{Re}_\infty}\left(\mu_l + \dfrac{\mu_{t_j}}{\sigma_\varepsilon}\right)\left(\dfrac{\partial \varepsilon}{\partial y}\right)_j dx_j \end{bmatrix} \tag{3.3.5}$$

$$\Phi_1 = \begin{bmatrix} \mathrm{Production_k} \\ \mathrm{Production_\varepsilon} \end{bmatrix} \tag{3.3.6}$$

$$\Phi_2 = \begin{bmatrix} \mathrm{Destruction_k} \\ \mathrm{Destruction_\varepsilon} \end{bmatrix} \tag{3.3.7}$$

$$\Phi_3 = \begin{bmatrix} \mathrm{Dilatation_k} \\ 0 \end{bmatrix} \tag{3.3.8}$$

For incompressible flows, Φ_3 vanishes. While calculating the turbulent convective flux, the convected properties are upwinded on the direction of the flow.

The explicit 3-stage Runge-Kutta scheme is also applied for the calculation of the time derivative tem of turbulence quantities in Equation(3.3.2).

3.4 Boundary Conditions

In this section, the boundary conditions applied in this study are explained. In aerodynamics, the most encountered boundaries are the wall and far-field inlet and outlet. The formulation and discretization for these boundary conditions are represented in the following sub-sections.

3.4.1 Far-Field Boundary Condition

Two types of far-field boundary are defined depending on the flow direction. If the flow is entering to the domain, the boundary is called as inlet boundary, otherwise it is an outlet boundary. The graphical representation of the inlet boundary is demonstrated in Figure 3.3.

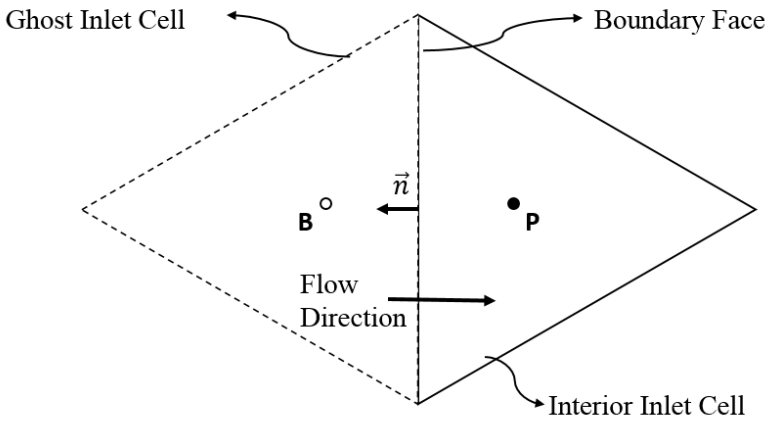

Figure 3.3. Far-Field Inlet Boundary

It is assumed that there is a ghost cell adjacent to the far-field inlet boundary in which the free stream values of the variables are stored. Therefore,

$$Q_B = \begin{bmatrix} \rho_\infty \\ \rho_\infty u_\infty \\ \rho_\infty v_\infty \\ \rho_\infty e_{T_\infty} \end{bmatrix} \tag{3.4.1}$$

and for the turbulence conservative variables

$$Q_{t_B} = \begin{bmatrix} \rho_\infty k_\infty \\ \rho_\infty \varepsilon_\infty \end{bmatrix} \tag{3.4.2}$$

Likewise, the pressure at the ghost inlet cell is equal to the free stream pressure.

$$p_B = p_\infty \tag{3.4.3}$$

The other far-field boundary type is encountered if the flow is leaving the domain, called as far-field outlet boundary. The outlet boundary is depicted in Figure 3.4.

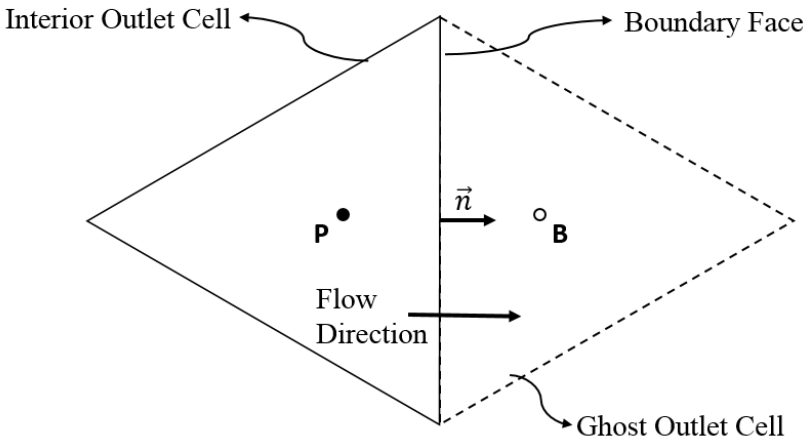

Figure 3.4. Far-Field Outlet Boundary

All variables but pressure at the ghost outlet cell center are equal to the interior outlet cell center values. Pressure is defined by user or taken as free stream pressure. Thus,

$$Q_B = \begin{bmatrix} \rho_P \\ \rho_P u_P \\ \rho_P v_P \\ \rho_P e_{T_P} \end{bmatrix} \tag{3.4.4}$$

and for turbulent properties

$$Q_{t_B} = \begin{bmatrix} \rho_P k_P \\ \rho_P \varepsilon_P \end{bmatrix} \tag{3.4.5}$$

Equation (3.4.3) is also applicable for the pressure at far-field outlet boundaries.

3.4.2 Wall Boundary Condition

Since turbulent flows are considered, no-slip condition is applied at the wall boundary. In addition, Neumann type boundary condition is performed for the turbulent kinetic energy. Therefore,

$$\left.\frac{\partial k}{\partial n}\right|_{\text{wall}} = 0 \tag{3.4.6}$$

are valid for this purpose.-The wall boundary type is presented in Figure 3.5.

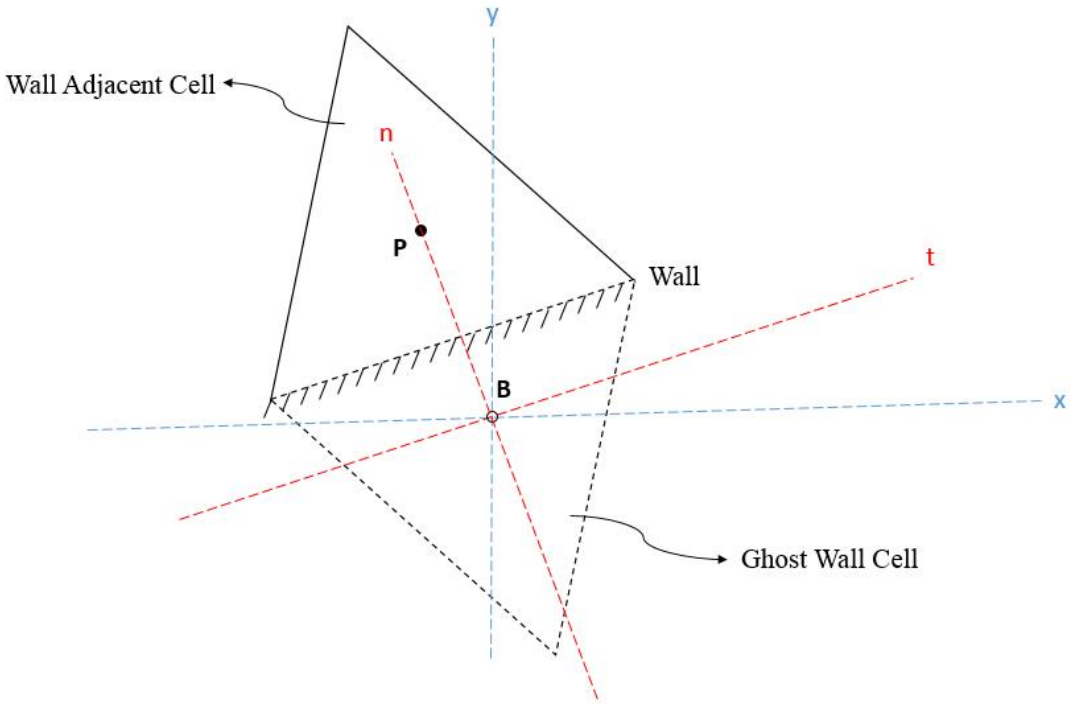

Figure 3.5. Wall Boundary

For the wall boundary condition, flow variables defined at the cell center of the ghost wall cell are:

$$Q_B = \begin{bmatrix} \rho_P \\ -\rho_P u_{n_P} \\ -\rho_P v_{t_P} \\ \rho_P e_{T_P} \end{bmatrix} \tag{3.4.7}$$

It is crucial to note that, the velocities at the ghost wall center are linked with the face normal and tangential components of the wall adjacent cell velocity. Pressure is also taken from the wall adjacent cell such that:

$$p_B = p_P \tag{3.4.8}$$

It is not that straightforward to describe the turbulence kinetic energy and its dissipation rate at the ghost wall cell center and the boundary conditions depend on the model used. Therefore, the details of wall boundary condition applied for the turbulence model equations are explained in Chapter 4 Near Wall Treatment.

3.5 Parallel Computations

Parallel computations are based on domain decomposition. In order to decompose the grid into partitions METIS-Serial Graph Partitioning and Fill-reducing Matrix Ordering [37] is used. A graph file which actually includes the neighbor connectivity of the cells is fed to METIS. The partitioning of the domain is achieved by using the kmetis program included in METIS software. During the partitioning, each cell is weighted by its number of edges so that each partition has about the same number of total edges to improve the load balancing in parallel computations.

The massage-passing libraries of Parallel Virtual Machine (PVM) are used in order to achieve the inter-process communication in a master-worker algorithm. In this algorithm, “the master” is responsible for performing input and output processes, starting PVM up, spawning the worker processes and sending the initial data to the workers. On the other hand, “the worker” solves the governing equations in the corresponding partition and applies the boundary conditions for both real boundaries and interface boundaries. The turbulent flow variables at the boundaries of partitions are exchanged between the neighboring partitions at each time step for interface boundary condition implementation.

CHAPTER 4

MODELING NEAR-WALL REGION

One of the most important problem for the turbulence models is the implementation of wall boundary condition since the turbulence is influenced by an adjacent wall. The presence of the wall in the flow domain damps the components normal to the wall, which in turn makes the turbulent flow anisotropic. The wall also causes the production of turbulence to increase through the shearing layer occurring in the flow.

In wall bounded flows, a boundary layer develops along the wall in which the velocity vanishes at the wall (no-slip condition) and reaches to its free stream value at the top. The highest gradients occurs at the near-wall region since the variation is largest. Since shear stress at the wall (or friction) is derived using the gradients of velocity and other flow properties, it is crucial to capture the near-wall accurately.

There exists mainly two methods in order to study the near-wall region. The standard method is to use a very fine grid resolution in the vicinity of wall so as to calculate the flow variables for these fine scales. This is an integration type methodology and requires a low-Reynolds-number (LRN) turbulence model. On the other hand, the increase in Reynolds number causes the region under the wall effect to decrease. But, the calculation of the gradients close to the wall is still quite important. At this point, an engineering approach is applied which introduces a function. This function constructs a bridge between the wall and the flow domain without a need for a very fine grid resolution, thus, reducing the computational cost significantly. This methodology is called wall function approach which requires a high-Reynolds-number (HRN) turbulence model.

4.1 Physics near the Wall

The near-wall region is generally divided into three layers [4]:

- Viscous sub-layer ($0 < y^+ < 5$)
- Buffer layer ($5 < y^+ < 30$)
- Fully turbulent region or inertial sub-layer ($y^+ > 30$)

where y^+ is dimensionless distance from the wall defined as

$$y^+ = \frac{\rho u_\tau y}{\mu} \tag{4.1.1}$$

Here u_τ is called as friction velocity which is represented as

$$u_\tau = \sqrt{\frac{\tau_w}{\rho}} \tag{4.1.2}$$

τ_w is used for the representation of wall shear stress.

Among these layers, turbulence is negligible in viscous sub-layer, whereas the viscous effects are quite small in the fully turbulent region. However, both viscous effects and turbulence are important in the buffer layer [29]. Depending on the distance from the wall the effects of turbulence and viscosity are given in Figure 4.1 obtained from DNS of a channel flow.

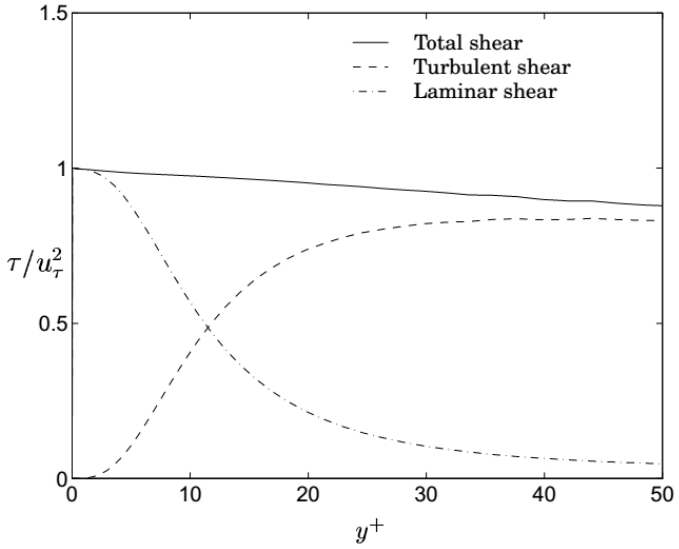

Figure 4.1. Laminar and Turbulent Shear in near-wall region [29]

4.1.1 Viscous sub-layer

In this region, flow is almost laminar and the molecular viscosity is dominant over the turbulent viscosity and plays an important role in momentum and heat transfer. The flow variables such as velocity, temperature and turbulence properties, like turbulence kinetic energy and its dissipation rate follow an asymptotic trend depending on the distance from the wall:

$$u^+ = \frac{U}{u_\tau} = y^+ \tag{4.1.3}$$

$$T^+ = \frac{T}{\left(T_w - T\right)\rho c_p u_\tau / q_w} = \Pr y^+ \tag{4.1.4}$$

$$k^+ = \frac{k}{u_\tau^{\,2}} = C_1 y^{+2} \tag{4.1.5}$$

$$\varepsilon^+ = \frac{\varepsilon\mu}{\rho u_\tau^{\,4}} = C_2 \tag{4.1.6}$$

where the constants are $C_1 = 0.1$ and $C_2 = 0.2$. The comparison of this model equations with the DNS of a channel flow is given in Figure 4.2. It can be seen from the figure that all the variables but turbulence kinetic energy yield similar results with DNS. However, turbulence kinetic energy is over-estimated. Therefore, this property should not be set a priori, but it should be solved.

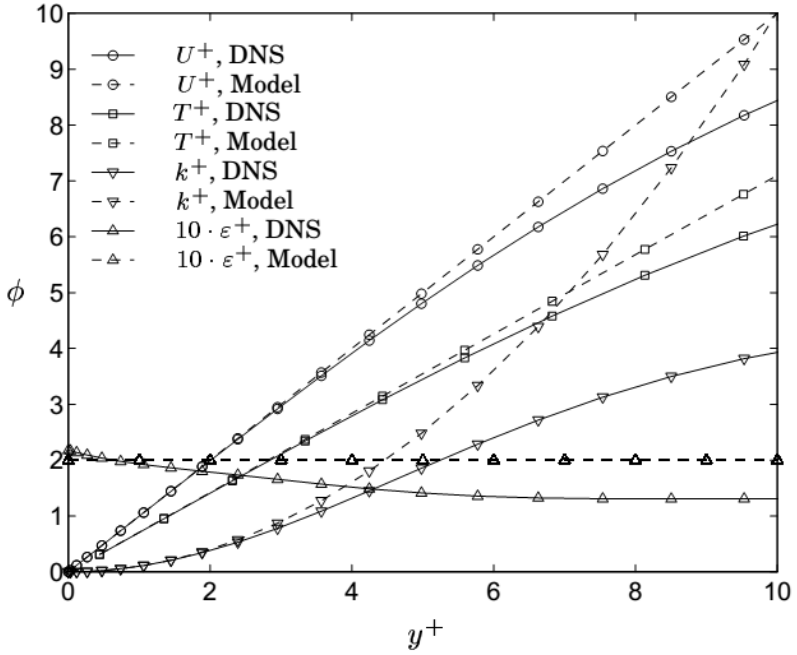

Figure 4.2. Near-wall variations of flow properties [29]

4.1.2 Fully Turbulent Region

In this region, beyond $y^+ > 30$, the variation of the properties are assumed to be [19]

$$u^+ = \frac{1}{\kappa} \ln y^+ + B \tag{4.1.7}$$

$$T^+ = \frac{1}{\kappa_T} \ln y^+ + B_T \tag{4.1.8}$$

$$k^+ = \frac{1}{\sqrt{C_\mu}} \tag{4.1.9}$$

$$\varepsilon^+ = \frac{\mu}{\rho u_\tau \kappa y} \tag{4.1.10}$$

where $\kappa = 0.41$, $C_\mu = 0.09$ and $B = 5$ are tuned by DNS-data. The coefficients for temperature are presented by Kays and Crawford [30] for air, such that $\kappa_T = \mathrm{Pr}_t / \kappa = 0.48$ and $B_T = 3.9$.

These models are also compared with the DNS data in Figure 4.3. Although velocity and temperature yield a great agreement, turbulent properties are less accurate.

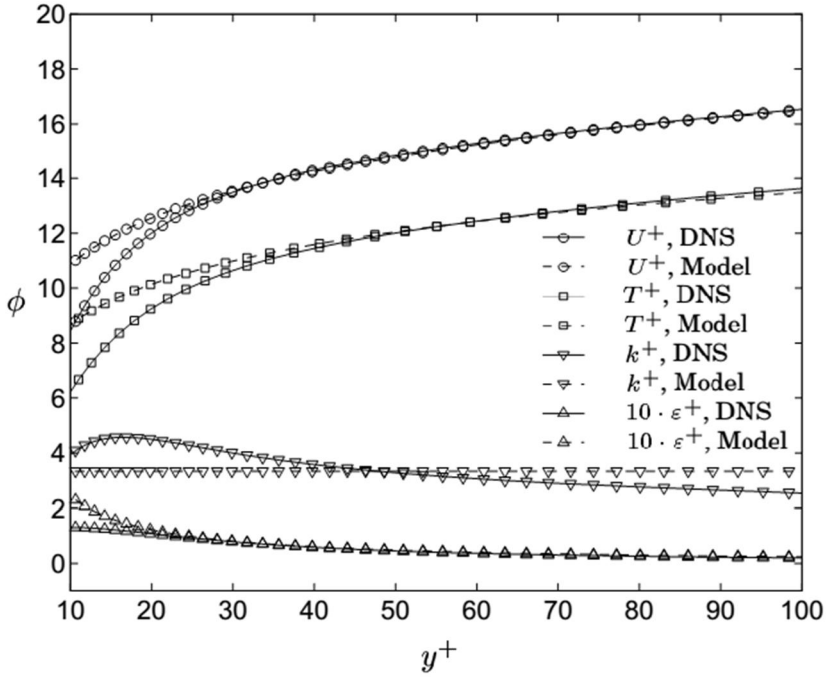

Figure 4.3. Fully turbulent region variations of flow properties [29]

4.1.3 Buffer Layer

From the latest DNS data, it can be seen that the maximum turbulence production is generated in the buffer layer. This also means that the largest variations in the turbulence source terms occurs in this layer which makes the modeling this region very difficult. Therefore, there is no general model in which the first computational node is placed in the buffer layer. Instead, the first near-wall node is located in either the fully turbulent region (HRN) or the viscous sub-layer (LRN).

4.2 Law-of-the-Wall

In the light of the prescribed variations of flow variables in the previous section, the law of the wall for the momentum can be summarized as given in Figure 4.4.

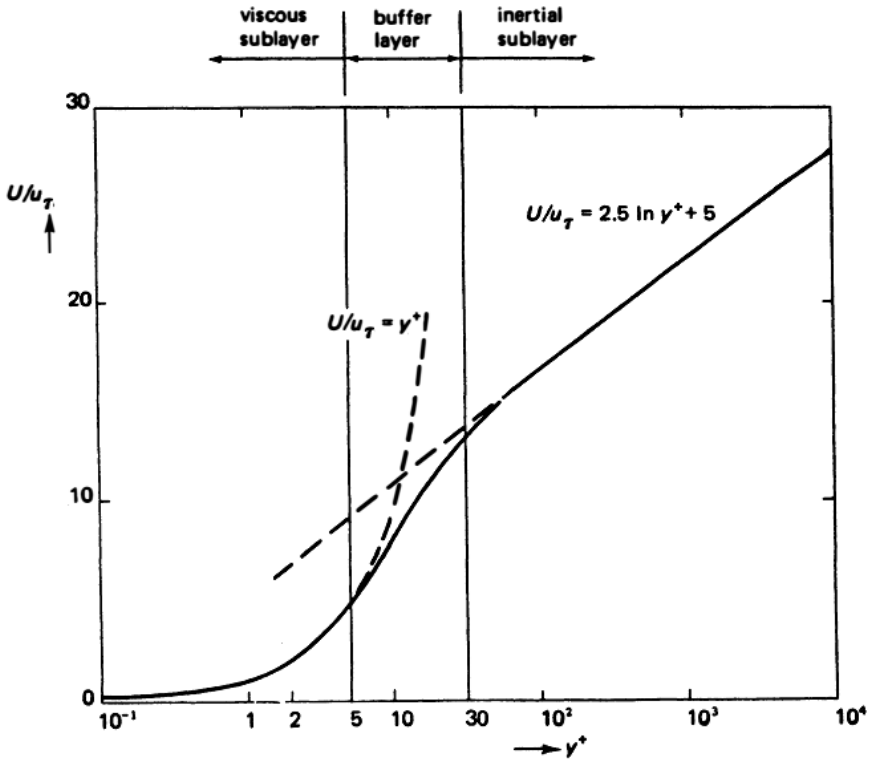

Figure 4.4. Log law of the Wall [4]

Here U/u_τ represents the non-dimensional velocity which is described in viscous sub-layer with the expression given in Equation (4.1.3) while in fully turbulent region Equation (4.1.7) is used to define it according to law-of-the-wall.

4.3 Wall Function Approach

In this study, a HRN-based model is applied for the modeling of turbulence near the walls. Wall functions are applied to predict the turbulence properties in the vicinity of the wall with relatively coarse near wall grid resolution. This approach avoids generating very fine grids close to the wall. The first near wall computational node (P) is placed in the fully turbulent region while adopting the mesh.

The wall function methodology proposed by Launder and Spalding [26] is implemented in order to avoid the weakness of standard wall functions' in predicting the re-circulating flows, where the turbulence kinetic energy becomes zero in separating and re-attachment points [29]. In this approach, the momentum equation in the first near-wall cell is solved with a modified viscosity, defined as:

$$\mu_{eff} = \frac{\rho C_\mu^{1/4} \sqrt{k_P}\, y_P \kappa}{\ln\left(E y_P^*\right)} \tag{4.3.1}$$

where $E = 9.793$ is an empirical constant and y_P^* is defined with k as

$$y_P^* = \frac{\rho_P C_\mu^{1/4} \sqrt{k_P}\, y_P}{\mu} \tag{4.3.2}$$

Then, the turbulence kinetic energy equation is solved for the wall adjacent cell with a modified integrated production term:

$$\text{Production}_k = \frac{\tau_w^{\,2}}{\rho \kappa C_\mu^{1/4} \sqrt{k_P}\, y_P} \tag{4.3.3}$$

Dissipation rate equation is not solved for the wall adjacent cell, instead it is set by using the following equation:

$$\varepsilon = \frac{u_\tau^{\,3}}{\kappa y} = \frac{C_\mu^{\,3/4} k_P^{\,3/2}}{\kappa y_P} \tag{4.3.4}$$

which is derived under the assumption of local equilibrium hypothesis which states that the production of turbulence kinetic energy and its dissipation rate are equal in the wall-adjacent control volume.

In the fully turbulent region laminar shear stress $\tau_l \equiv \mu_l \partial U / \partial y$ is negligible and, assuming the shear stress is constant through the wall adjacent cell, the turbulent shear stress, τ_t is equal to the wall shear. Wall shear stress is defined by the effective viscosity given in Equation (4.3.1):

$$\tau_w = \frac{\rho C_\mu^{\,1/4} \sqrt{k_P}\kappa}{\ln\left(E y_P^{\,*}\right)} u_P \tag{4.3.5}$$

Chieng and Launder [34] improved the above methodology by taking into account of viscosity-affected region. In this model, turbulent kinetic energy is assumed to be varying as a parabolic function. This assumption proposes that in the viscous sublayer, the fluctuating velocity increases linearly with the distance from wall. However, the turbulent shear stress is zero within the viscous sublayer since turbulent viscosity is dominated by the molecular viscosity. Just over the viscous sublayer turbulent shear stress undergoes an abrupt increase and varies linearly over the top of the cell. This physical assumption is depicted in Figure 4.5 where y_v represents the edge of the viscous sublayer and y_n is the maximum distance of the cell faces to the wall.

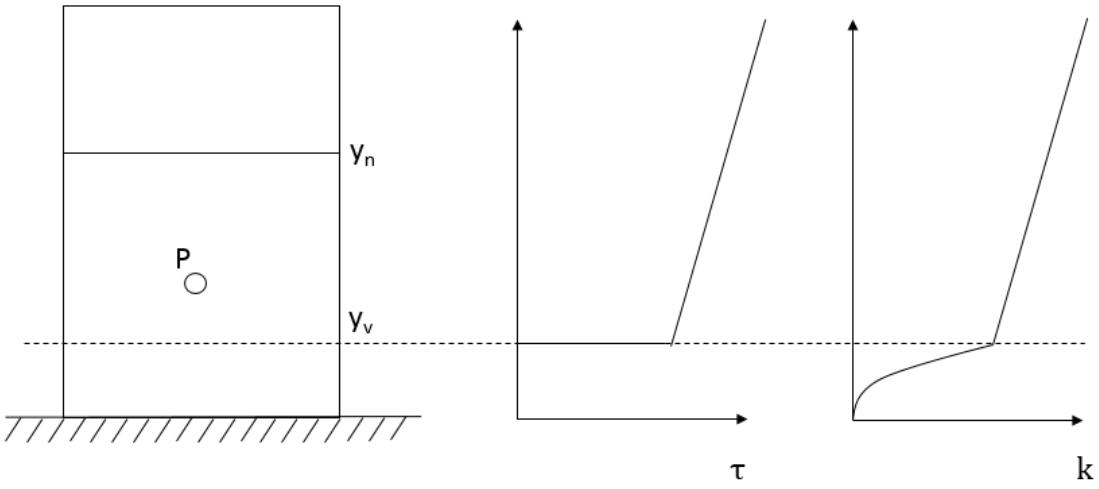

Figure 4.5. Variation of Variables in the Wall Adjacent Cell, Chieng-Launder Model

In this model, the near-wall cell is divided into two sublayers: viscous sublayer next to the wall and fully turbulent region away from the wall. Since turbulent viscosity is assumed to be zero within the viscous sublayer, production of turbulence kinetic energy vanishes in this region. The thickness of the viscous sublayer is assumed to be related to a dimensionless wall distance parameter $y_v^* = 20$.

$$y_v = \frac{\mu y_v^*}{\rho c_\mu^{1/4} k_P^{1/2}} \tag{4.3.6}$$

The average of the production of turbulence kinetic energy over the near wall cell is obtained using the below equation:

$$\text{Production}_k = \frac{\tau_w^{\,2}}{\rho \kappa C_\mu^{1/4} \sqrt{k_P}\, y_n} \ln\left(\frac{y_n}{y_v}\right) \tag{4.3.7}$$

The dissipation rate of turbulence kinetic energy is assumed to be remain constant in the viscous sublayer and it is same as given by Equation(4.3.4) within the fully turbulent

region. The cell-averaged dissipation rate for calculating the transport equation of turbulence kinetic energy is obtained as

$$\bar{\varepsilon} = \frac{1}{y_n}\left[\frac{c_\mu^{3/4} k_P^{3/2}}{\kappa y_v} + \frac{c_\mu^{3/4} k_P^{3/2}}{\kappa} \ln\left(\frac{y_n}{y_v}\right)\right] \tag{4.3.8}$$

Similar to Launder-Spalding model, the transport equation for dissipation rate is not solved in the wall-adjacent cell. Instead, the value of dissipation rate in near-wall cells are computed by using Equation(4.3.4).

4.4 Near Wall Modeling Approach

Near wall models are based on LRN approach for which the flow field is calculated directly down to the wall. This methods requires very fine grids in vicinity of the wall, i.e. $y^+ \approx 1$. The sense that these models make is that they use damping functions to predict the damping effects of presence of wall in the flow field. These damping functions are 1 for wall functions, however, they are related to non-dimensional turbulent properties for LRN models. In this study, Abid's model [38] and Abe-Kondoh-Nagano [39] model are applied for near wall treatment

4.4.1 Abid's k-ε Turbulence Model

The damping function suggested by Abid [38] are given in Table 4.1.

Table 4.1. Damping functions for Abid's Model

f_μ	f_1	f_2
$\tanh\left(0.008\,\mathrm{Re}_k\right)\left(1+\frac{4}{\mathrm{Re}_t^{3/4}}\right)$	1.0	$1-\frac{2}{9}\exp\left(-\frac{\mathrm{Re}_t^2}{36}\right)\left(1-\exp\left(-\frac{\mathrm{Re}_k}{12}\right)\right)$

where the non-dimensional turbulent Reynolds numbers are defined such that

$$\mathrm{Re}_k = \frac{\rho y k^{1/2}}{\mu} \tag{4.4.1}$$

$$\mathrm{Re}_t = \frac{\rho k^2}{\mu \varepsilon} \tag{4.4.2}$$

The boundary conditions at the wall is the other important parameter for LRN number. In Abid's model both the velocities and turbulent kinetic energy is set to zero while dissipation rate of turbulence kinetic energy at the wall is as follows:

$$\varepsilon_w = \frac{\mu}{\rho}\frac{\partial^2 k}{\partial n^2} \tag{4.4.3}$$

4.4.2 Abe-Kondoh-Nagano Turbulence Model

In order to calculate the complex turbulent flows and heat transfer in separating and reattaching flows, Abe, Kondoh and Nagano [39] suggests a turbulence model which is known as AKN model in literature. They introduce the Kolmogorov velocity scale u_ε instead of friction velocity u_τ to account for the near-wall and LRN effects in attached and detached flows. The damping functions for AKN model is presented in Table 4.2.

Table 4.2. Damping functions for AKN Model

f_μ	f_1	f_2
$\left\{1-\exp\left(-\frac{y_\varepsilon^*}{14}\right)\right\}^2 \times\left[1+\frac{5}{\mathrm{Re}_t^{3/4}}\exp\left\{-\left(\frac{\mathrm{Re}_t}{200}\right)^2\right\}\right]$	1.0	$\left\{1-\exp\left(-\frac{y_\varepsilon^*}{3.1}\right)\right\}^2 \times\left[1-0.3\exp\left\{-\left(\frac{\mathrm{Re}_t}{6.5}\right)^2\right\}\right]$

The non-dimensional wall distance is defined by Kolmogorov velocity scale such that

$$y_{\varepsilon}^{*} = \frac{\rho u_{\varepsilon} y}{\mu} \tag{4.4.4}$$

where u_{ε} is

$$u_{\varepsilon} = \left(\frac{\mu \varepsilon}{\rho} \right)^{1/4} \tag{4.4.5}$$

The boundary conditions applied at the wall is similar to Abid's model, but ε_w is defined as

$$\varepsilon_w = \frac{2\mu}{\rho} \left(\frac{\partial \sqrt{k}}{\partial n} \right)^2 \approx \frac{2\mu}{\rho} \frac{k_P}{{y_P}^2} \tag{4.4.6}$$

CHAPTER 5

RESULTS AND DISCUSSIONS

In this chapter, validation of the developed turbulent flow solver is presented in this chapter. For this purpose, turbulent flat plate case is studied, first. The flow over RAE 2822 transonic airfoil and NACA 0012 are solved using the implemented turbulent models. The near-wall characteristics are compared with experimental data and a commercial CFD solver, Fluent.

5.1 Validation of the Solver

For the validation of the implementation of k-ε turbulence model to the base flow solver, flow over a turbulent flat plate and RAE 2822 are studied.

5.1.1 Turbulent Flat Plate Solutions

In order to assess the accuracy of the k-ε turbulence model implemented in the HYP2D code, first, a simple turbulent flat plate case is studied. The flow conditions are given in Table 5.1.

Table 5.1. Flow Conditions over for the Turbulent Flat Plate Case

M_∞	0.2
α	0°
Re	4.8 x 10^6

For this incompressible case, a fully quadrilateral grid is generated by using GAMBIT. The problem is also solved using the popular commercial CFD solver Fluent with the same grid. The boundary conditions and the grid generated are represented in Figure 5.1.

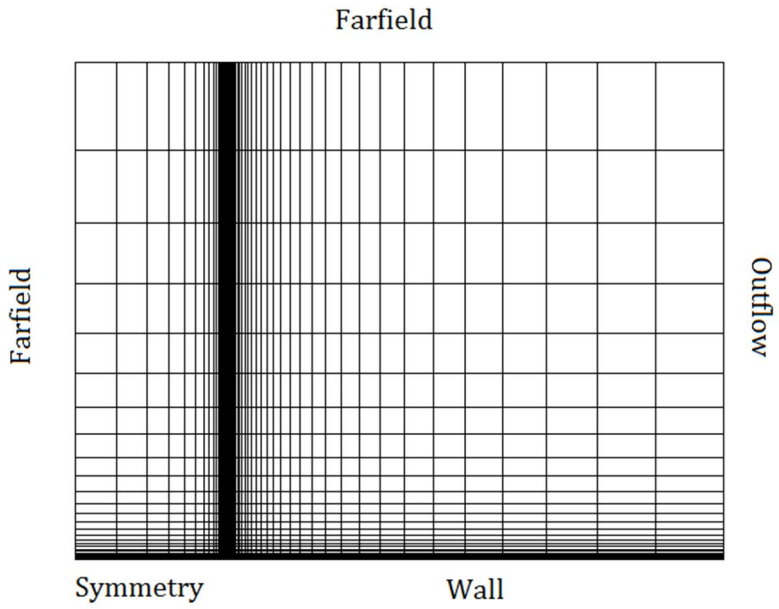

Figure 5.1. Grid Generated for Turbulent Flat Plate Case

The above grid can be used for only to obtain solutions using wall functions since the near wall resolution is about order of $y^+ \approx 80$. In order to test the LRN models, a quite fine mesh resolution is performed in the near-wall region. Near-wall grid resolutions for wall functions and LRN models are compared in Figure 5.2 at the same portion of the solution domain. It can be seen that, for the LRN models one should put the first computation node about 100 times lower than the one put for wall function models.

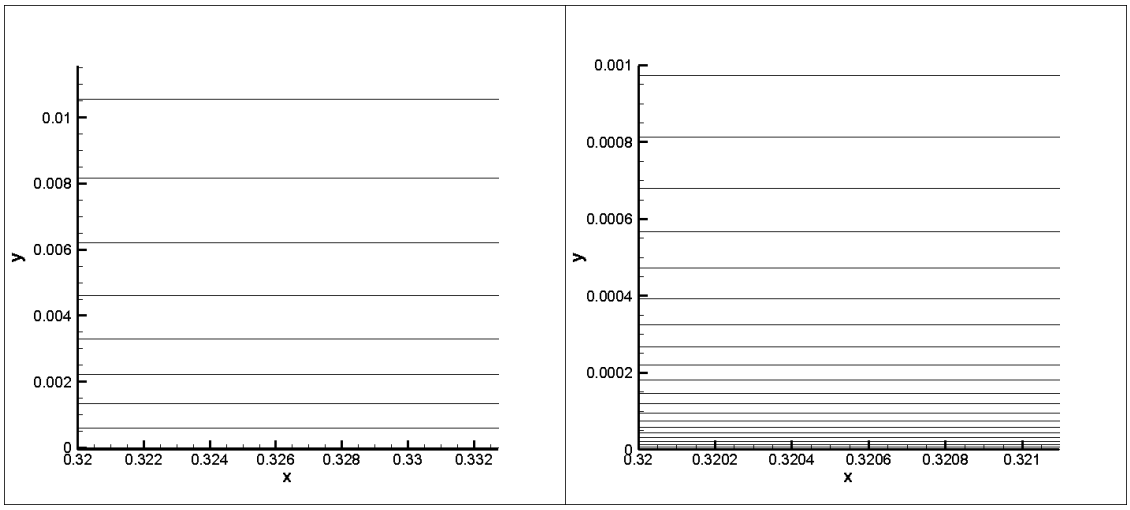

Figure 5.2. Near-Wall Grid Resolutions for Wall Functions and LRN Models

The solutions are performed for the free stream conditions given in Table 5.1 both by using wall function approach and the LRN near-wall modeling approach. The same models are also used for the calculations performed by Fluent.

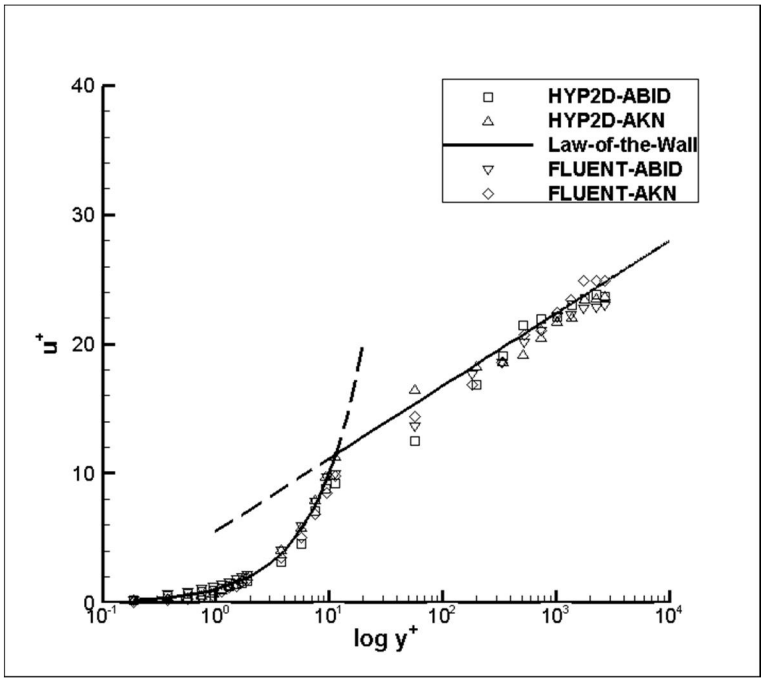

Figure 5.3. Velocity Profile in the Boundary Layer at x=0.4 (LRN Models)

One of the most important parameter in terms of validation of a turbulence model in wall-bounded flows is the boundary layer velocity profile. The velocity profile in the boundary layer which is developed over a flat plate obeys the law-of-the-wall (See Chapter 4.2). Therefore, the velocity profile results obtained over the flat plate at x=0.4 are compared with the law-of-the-wall. Figure 5.3 shows the convenience of the LRN model solutions with the law-of-the-wall. In addition, the results show good agreement with the results of Fluent software in which the same LRN models are applied.

In Figure 5.4, the results obtained from the simulations using Launder-Spalding Wall Function and Chieng-Launder Wall Function methods are compared with both law-of-the-wall and Fluent's Wall Function method applied for the near-wall treatment in k-ε turbulence model. Since, the center of the first computational cell next to the wall is placed in the fully turbulent region, one should expect that the comparison is to be performed in that region. This argument is completely true for computational means, however, the velocity profile in the viscous sublayer can be approximated using the wall shear stress. In viscous sublayer, wall shear stress can be calculated using the following equation.

$$\tau_w = \mu \frac{\partial U}{\partial y} \tag{5.1.1}$$

As stated in Chapter 4.3, the wall shear stress is computed with Equation(4.3.5). Therefore, $\partial U/\partial y$ can easily be calculated with assuming wall shear stress is constant throughout the viscous sublayer. Applying this procedure the velocity profile in the viscous sublayer can be obtained. It can be clearly seen that the velocity profiles over the turbulent flat plate obtained from the k-ε turbulence model with wall functions are in good agreement with the law-of-the-wall even in viscous sublayer.

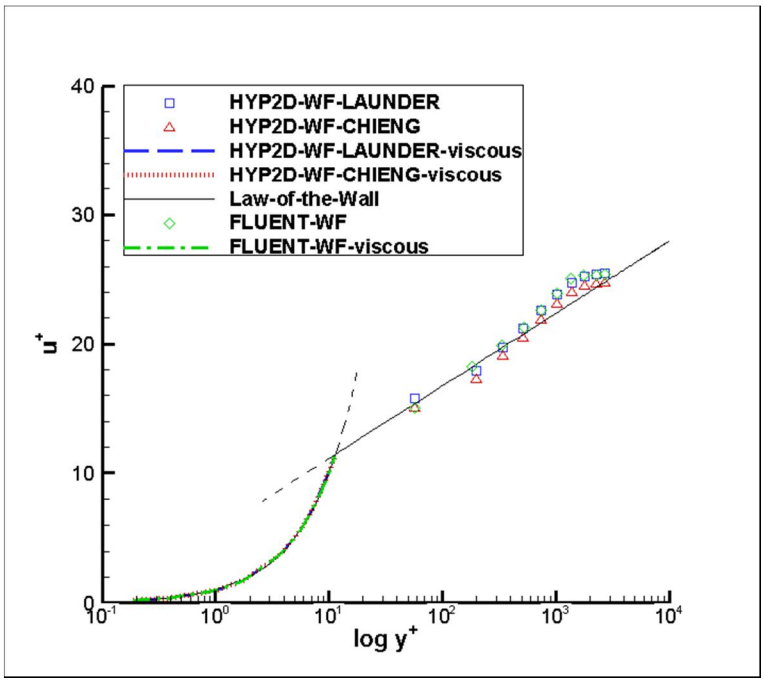

Figure 5.4. Velocity Profile in the Boundary Layer at x=0.4 (Wall Functions)

In order to validate the implementation of the turbulence models in HYP2D code skin friction coefficients through the flat plate are compared. The comparison are performed using the same strategy given above. First, LRN models are compared with each other and the theoretical data which is taken from White's fluid mechanics book [34]. Then, the values are checked whether the LRN models yield similar results with Fluent. Figure 5.5 shows the skin friction coefficient over the flat plate which is calculated using following expression:

$$C_f = \frac{\tau_w}{0.5\rho U_\infty} \tag{5.1.2}$$

The results point out that the skin friction coefficients obtained by the LRN models are quite similar to theoretical data. However, Abid's model calculates the wall shear stress higher.

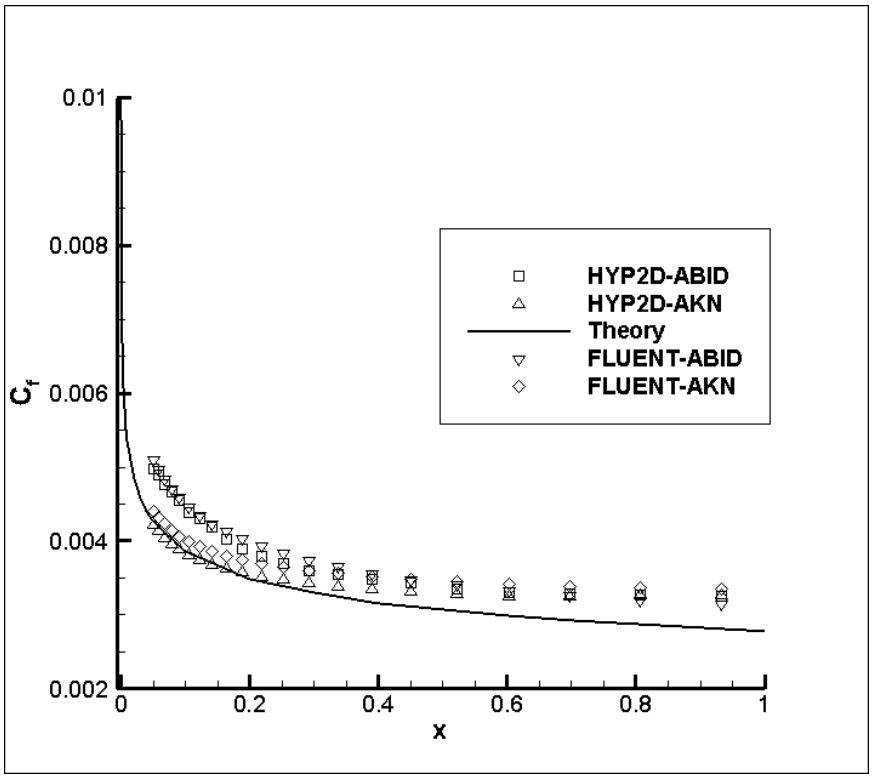

Figure 5.5. Skin Friction Coefficient over the Flat Plate (LRN Models)

It can be seen from Figure 5.6 that the Wall Function results are in the same fashion with the LRN models'. The results are in agreement with Fluent and theoretical skin friction coefficient.

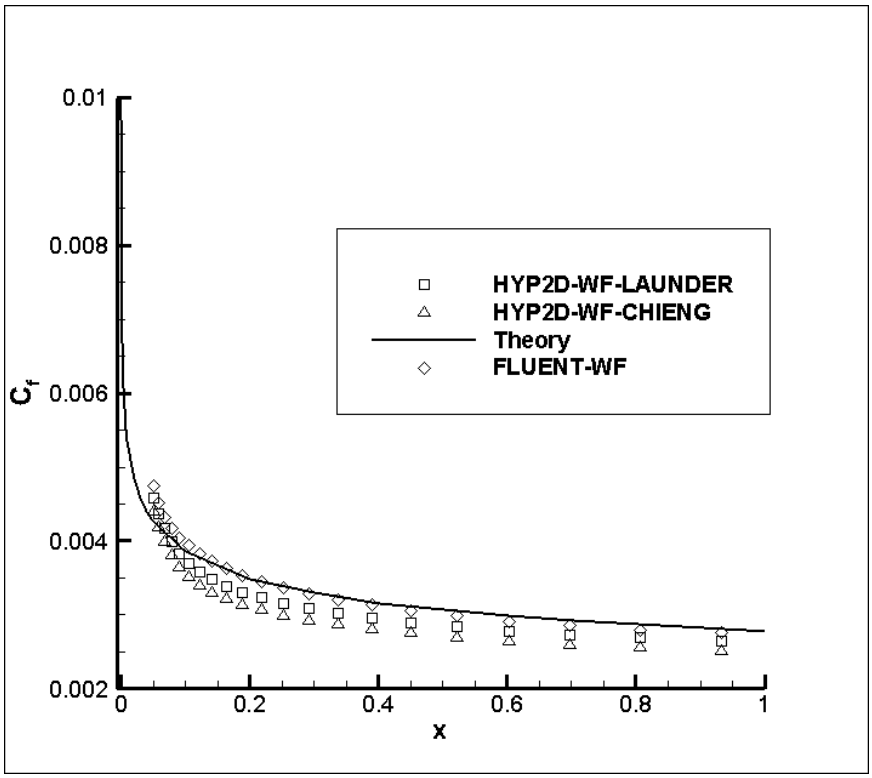

Figure 5.6. Skin Friction Coefficient over the Flat Plate (Wall Functions)

5.1.2 RAE 2822 Airfoil Solutions

The RAE 2822 airfoil was tested at several conditions by Cook, McDonald and Firmin [35]. The experimental data include the boundary layer velocity profile, pressure coefficient distribution, skin friction coefficient distribution and velocity profile at wake region. This rich database makes RAE 2822 an attractive choice for turbulence modelers for validating their models and implementation. In this study, a detailed comparison performed using different near-wall approaches for k-ε turbulence model.

The test case presented here corresponds to Case 9 of the referenced experiment set. The tests are conducted at an angle of attack of 3.19°. The tunnel corrected angle of attack is

taken as 2.8° which is suggested by Coakley [36]. The flow conditions for the RAE 2822 case is given in Table 5.2.

Table 5.2. Flow Conditions for RAE 2822 Airfoil Simulations

M_∞	0.73
α	2.8°
Re	6.5 x 10^6

Two C-type hybrid grids are generated for the solutions over RAE 2822 airfoil, one for the LRN models and the other for the Wall Functions. The boundary layer is composed of quadrilateral control volumes and remaining is meshed by triangular control volumes. The total grid size is 36710 for the Wall Function solutions and 48500 for the LRN models. The grid extends approximately 20 chords from the airfoil and is divided into 8 partitions for the parallel computing. In order to avoid grid dependency of the solution 5 grid domain are generated for wall function solutions and LRN model solutions. The number of points placed on the airfoil upper surface are selected as the comparison parameter for grid independency. The resultant lift and drag coefficients for different grid size and grid resolution on the upper surface of airfoil are compared in Figure 5.7 until the results do not change. It is decided to study with a grid where the airfoil surface consists of 160 intervals since Cl and Cd values does not change for grids which have more intervals. The grid generated for RAE 2822 simulations with wall function method is represented in Figure 5.8.

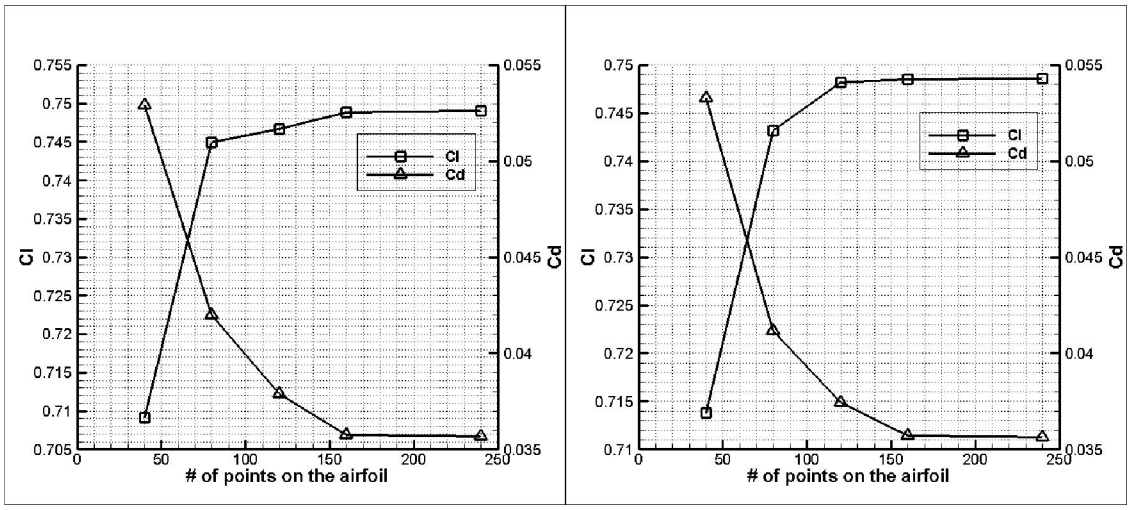

Figure 5.7. Grid Independency Study for RAE 2822 Simulations (left: LRN models, right: Wall Function models)

First, the flow field is represented for the transonic airfoil with a comparative point of view by using the same color scale for all turbulence models. Mach number contours around the airfoil under given flow conditions are represented for Abid's model, AKN model and wall functions in Figure 5.9, Figure 5.10 and Figure 5.11, respectively. Although the contour plots seem quite comparable for all models, it can be stated that the shock formation on the upper surface of airfoil is captured smoothly by Abid's model while AKN model and wall functions show a sharper shock profile. Morever, Abid's model is less dissipative than other models in terms of velocity. All models show good agreement with the results obtain by Fluent.

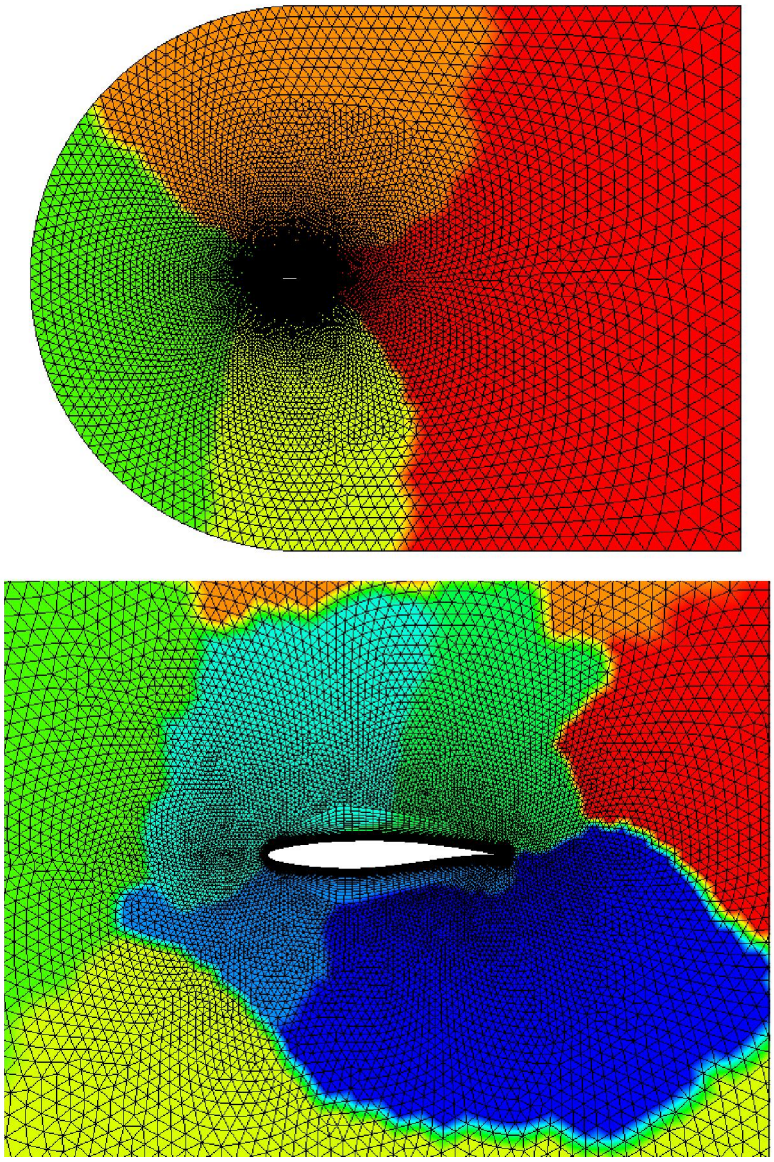

Figure 5.8. Grid for RAE 2822 Simulations

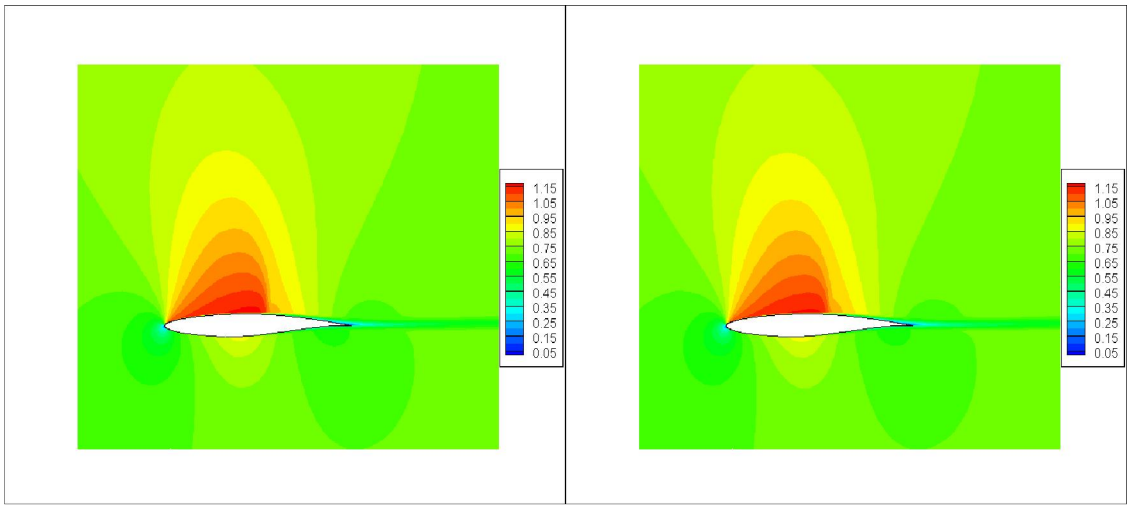

Figure 5.9. Comparison of Mach Contours-Abid's Model (left: HYP2D, right: Fluent)

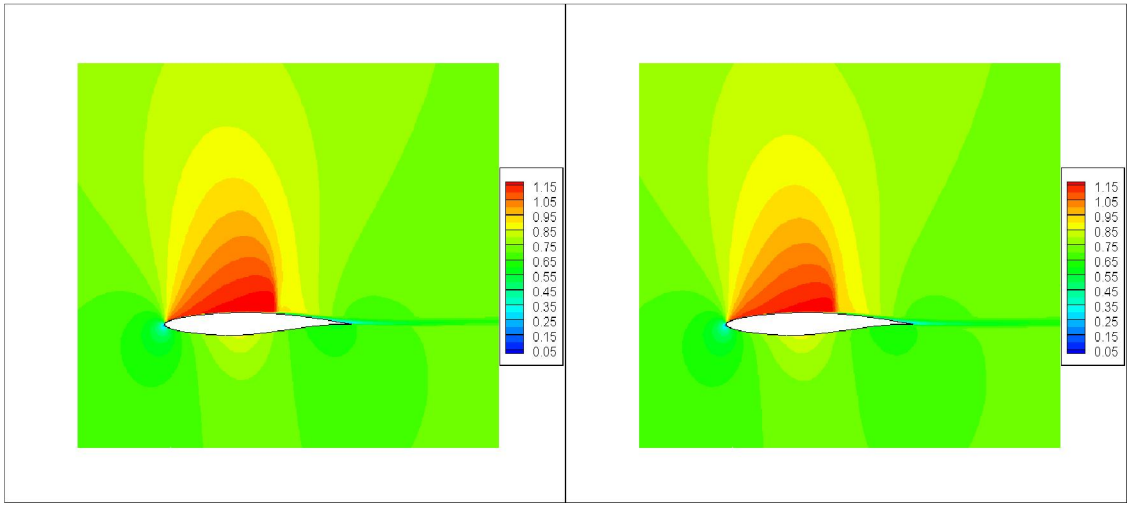

Figure 5.10. Comparison of Mach Contours-AKN Model (left: HYP2D, right: Fluent)

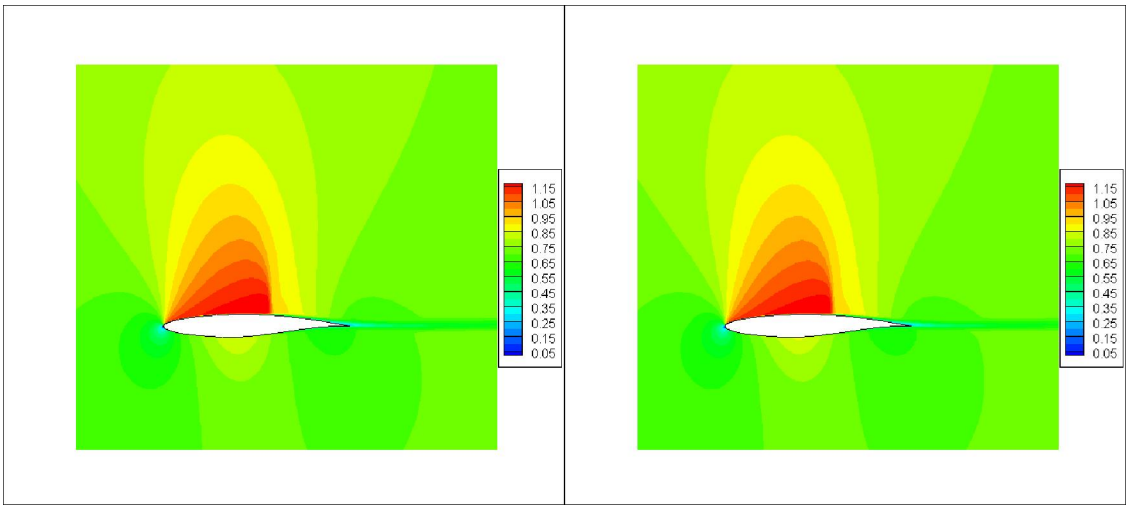

Figure 5.11. Comparison of Mach Contours-Wall Function (left: HYP2D, right: Fluent)

The turbulence kinetic energy distribution around the airfoil is given with contour plots by comparing the Fluent's solution. Like Mach number contours, turbulence kinetic energy fields are represented in a 2-column figure in which HYP2D solutions are given on the left and Fluent on the right in Figure 5.12, Figure 5.13 and Figure 5.14 for Abid's model, AKN model and wall functions respectively. The comparisons with the Fluent results are quite successful for all models. However, AKN model underpredicts the turbulence kinetic energy on the lower surface of airfoil. This results to a fast destruction of turbulence kinetic energy just behind the trailing edge. The dissipation of energy at the wake region takes longer for the other models.

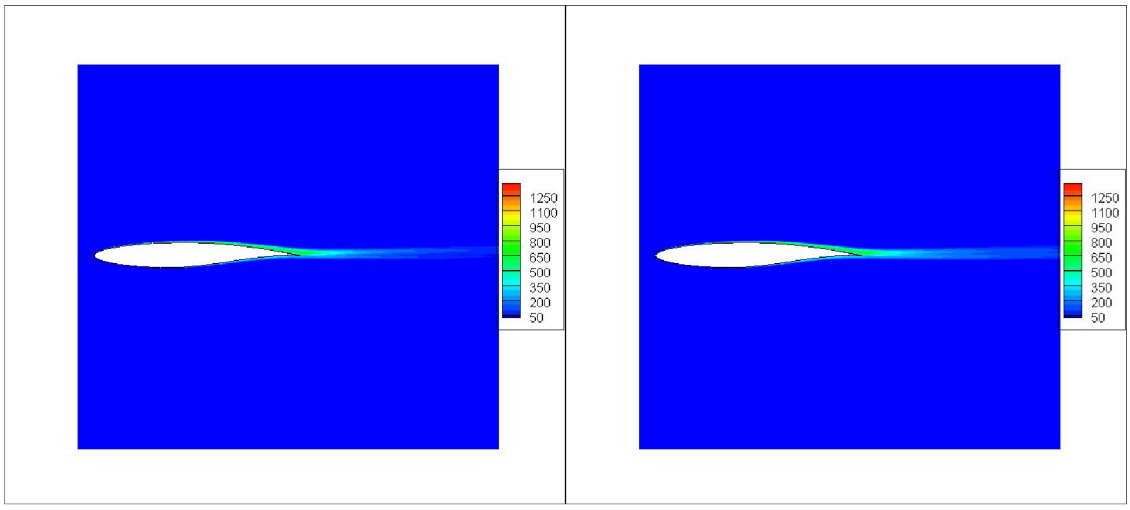

Figure 5.12. Comparison of Turbulence Kinetic Energy [m^2/s^2] Contours-Abid's Model (left: HYP2D, right: Fluent)

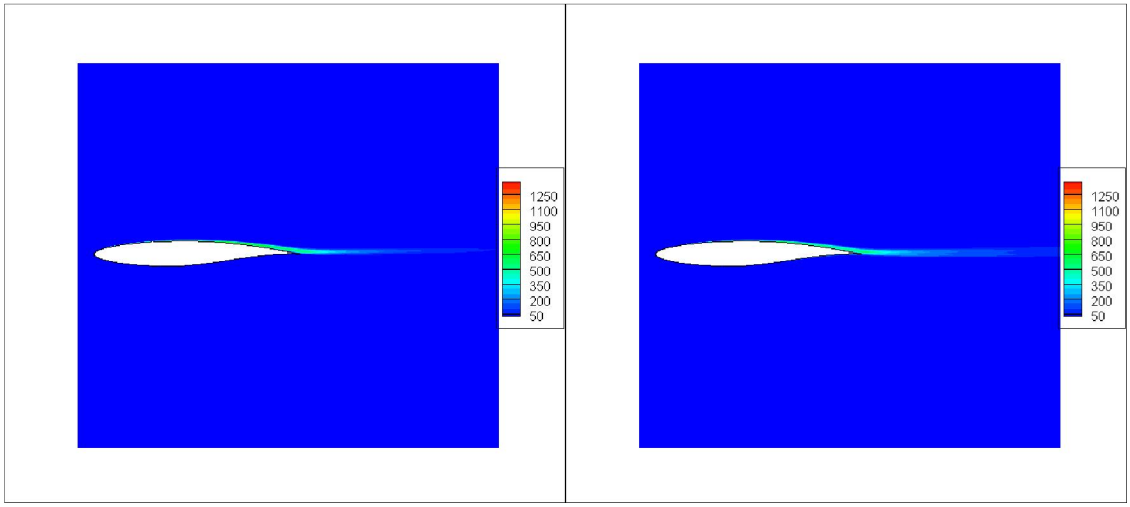

Figure 5.13. Comparison of Turbulence Kinetic Energy [m^2/s^2] Contours-AKN Model (left: HYP2D, right: Fluent)

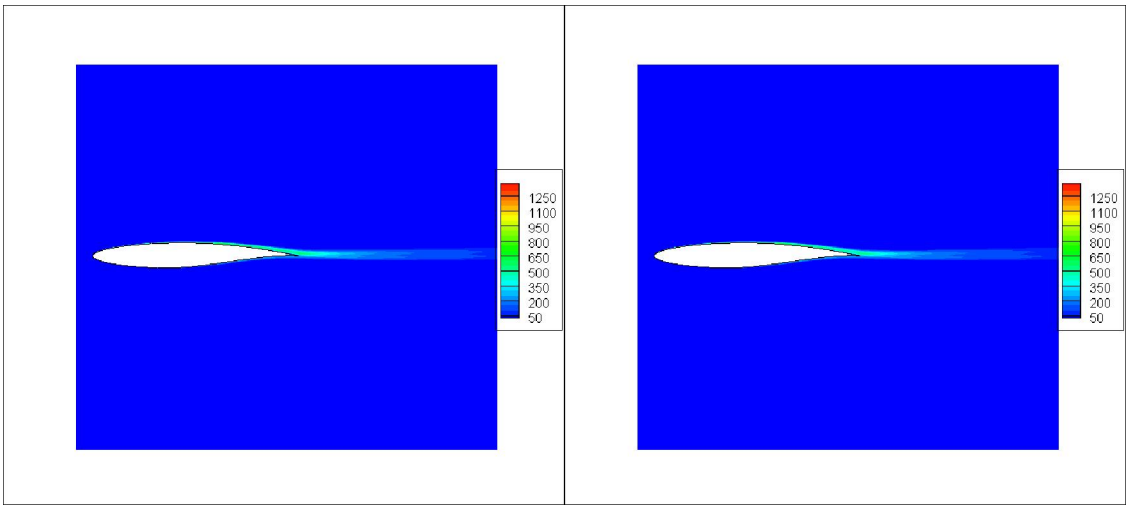

Figure 5.14. Comparison of Turbulence Kinetic Energy [m^2/s^2] Contours-Wall Function (left: HYP2D, right: Fluent)

The other important parameter is turbulent viscosity which affects the momentum of the flow directly for viscous flows. Turbulent viscosity fields around the airfoil and at the wake region are given in Figure 5.15, Figure 5.16 and Figure 5.17. The contour plots show that AKN model underpredicts the turbulent viscosity at the wake region. In addition, the turbulent viscosity values obtained at the wake region of airfoil using HYP2D are a little bit smaller than predictions of Fluent resulting to narrower band of turbulent viscosity effected region.

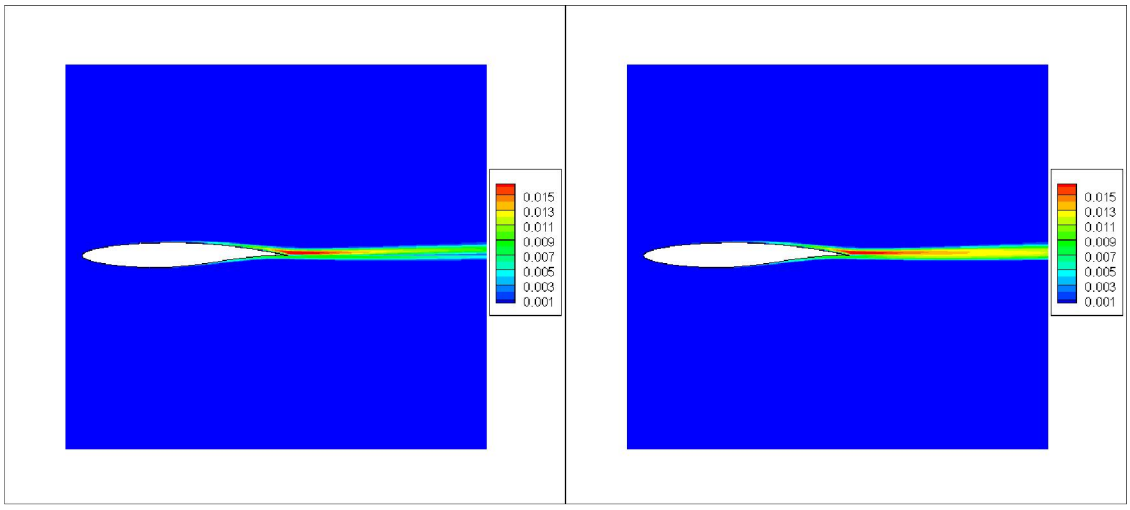

Figure 5.15 Comparison of Turbulent Viscosity [kg/m s] Contours-Abid's Model (left: HYP2D, right: Fluent)

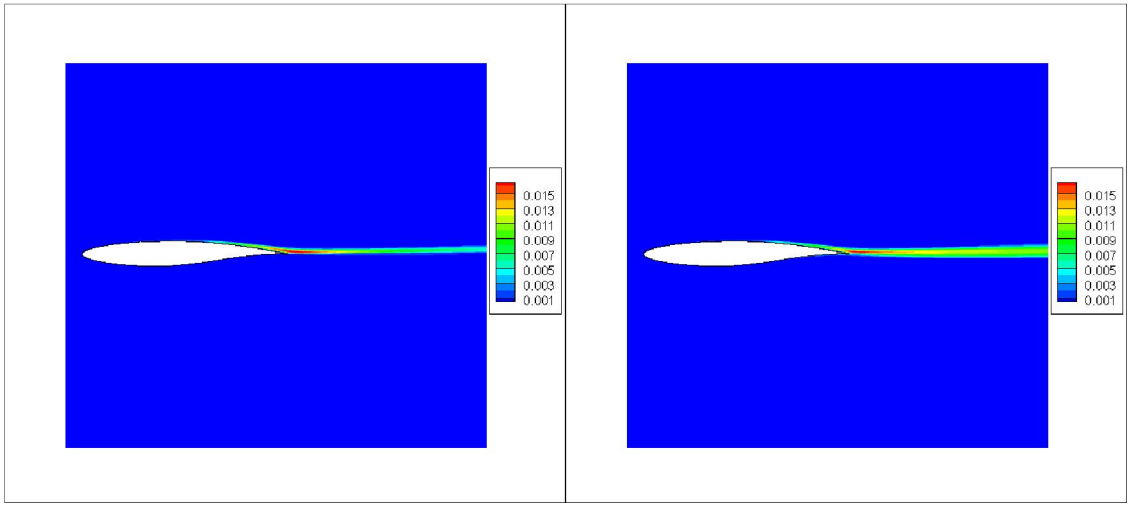

Figure 5.16. Comparison of Turbulent Viscosity [kg/m s] Contours-AKN Model (left: HYP2D, right: Fluent)

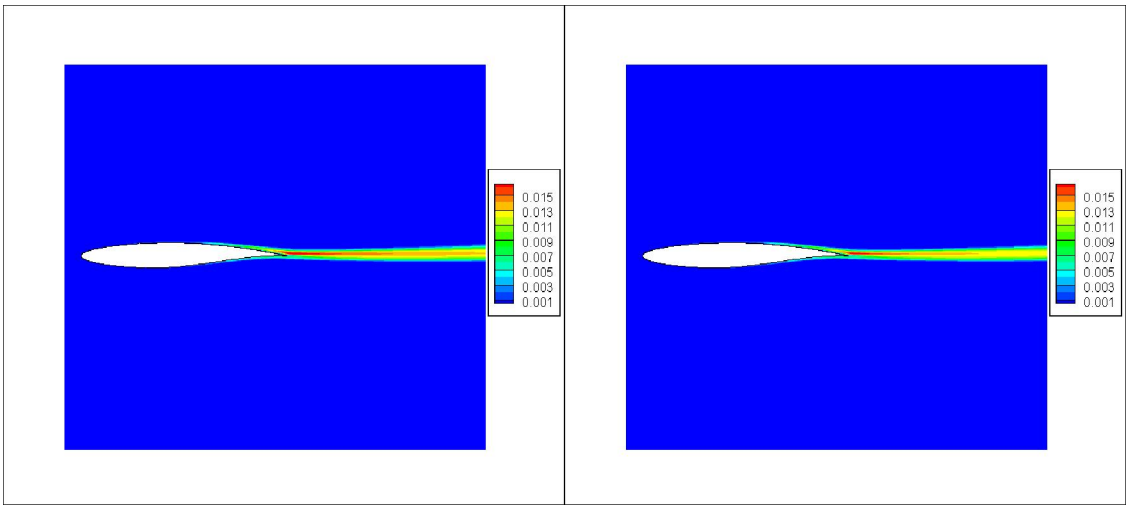

Figure 5.17. Comparison of Turbulent Viscosity [kg/m s] Contours-Wall Function (left: HYP2D, right: Fluent)

After presenting and comparing the flow field around RAE 2822, the boundary layer velocity profile on the upper surface of the airfoil is assessed. Similar to the flat plate case, the LRN and HRN type models are compared with models which are members of their own groups. The results are also checked with the experimental data and the results obtained from Fluent. In addition, the boundary layer profile is compared with the solutions obtained from the simulations performed using the Spalart-Allmaras turbulence model which has been already implemented in HYP2D. The velocity profiles normalized by the velocity at the edge of the boundary layer at x/c=0.404, x/c=0.574, x/c= 0.750 and x/c=0.900 in Figure 5.18, Figure 5.19, Figure 5.20 and Figure 5.21, respectively. It can be stated that, Abid's model fits best to the experimental data among k-ε turbulence models. However, Spalart-Allmaras model seems to be more successful in predicting the velocity profile in the near-wall region. All models are convenient with the experimental data for x/c=0.404, x/c=0.574, however, the convenience is lost near the trailing edge, although LRN models and Spalart-Allmaras model show agreement at this region. This region is likely to be the region behind the shock.

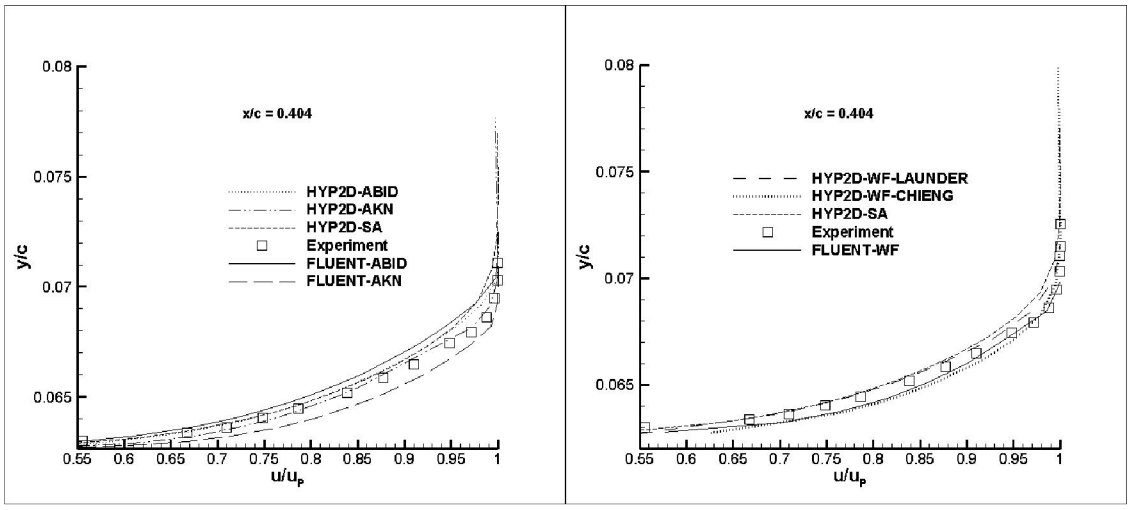

Figure 5.18. Boundary Layer Velocity Profile over RAE 2822 at x/c=0.404

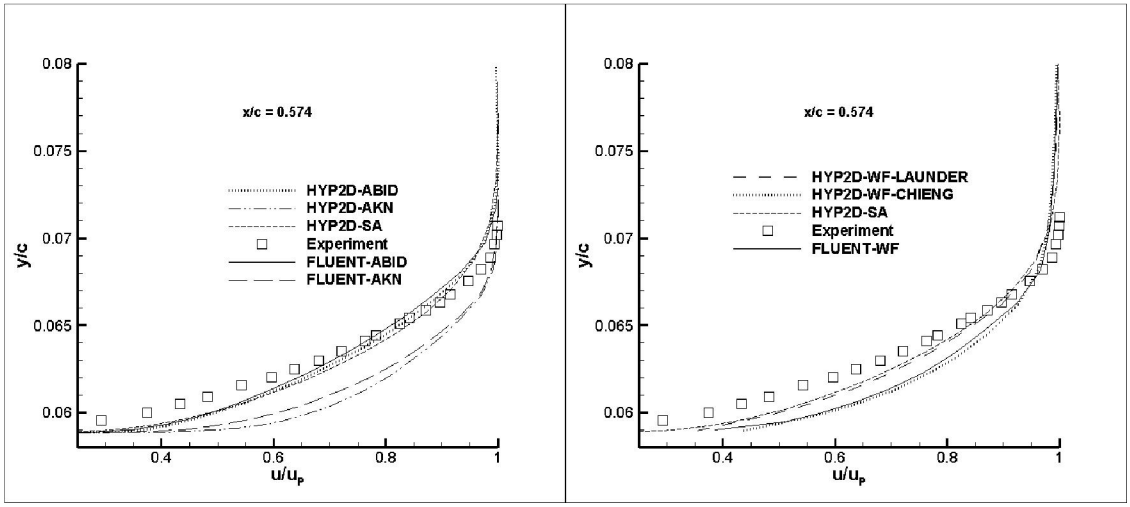

Figure 5.19. Boundary Layer Velocity Profile over RAE 2822 at x/c=0.574

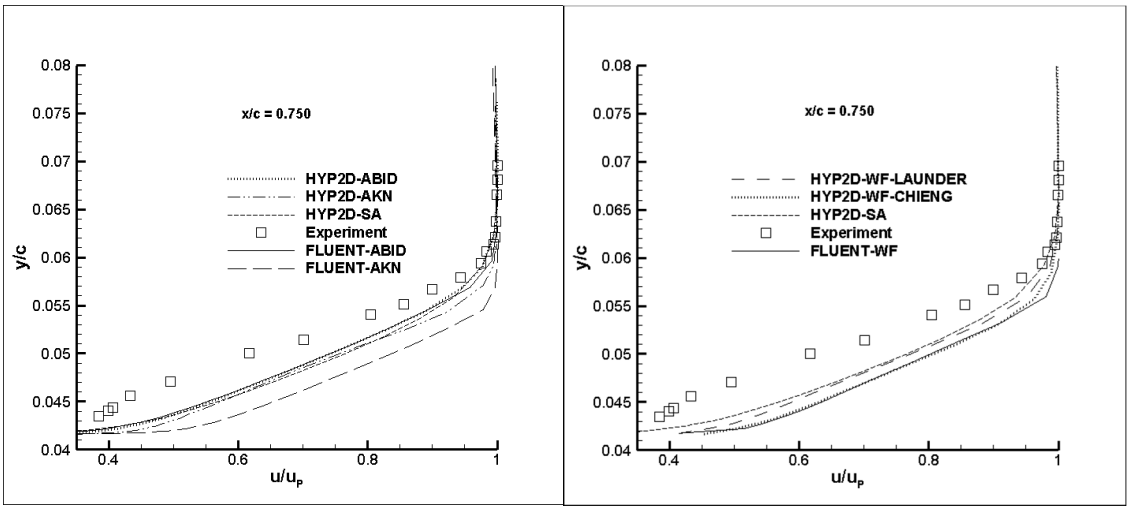

Figure 5.20. Boundary Layer Velocity Profile over RAE 2822 at x/c=0.750

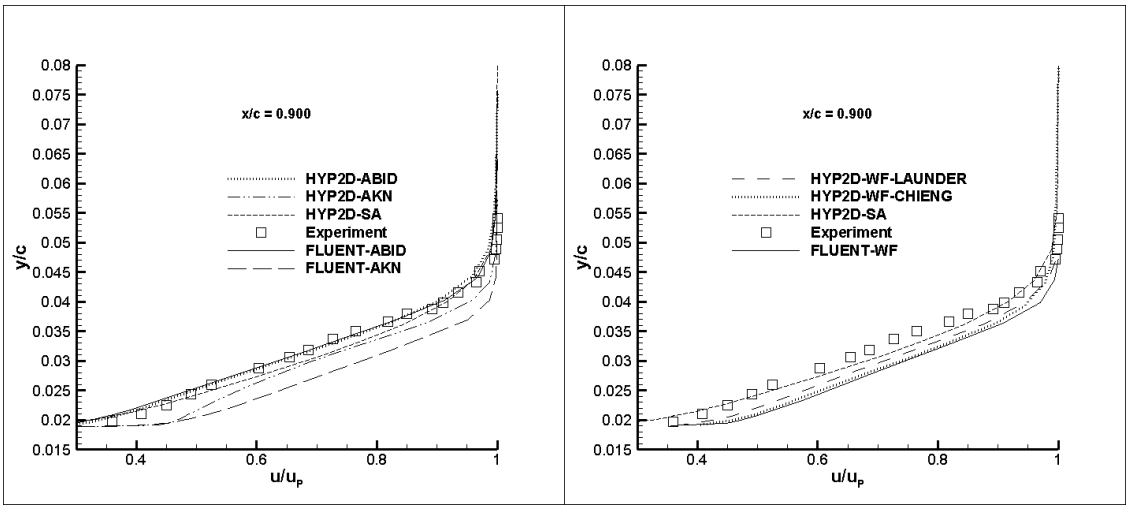

Figure 5.21. Boundary Layer Velocity Profile over RAE 2822 at x/c=0.900

Pressure coefficient distributions are represented in Figure 5.22. The wall function models of Launder-Spalding and Chieng-Launder are in a good agreement with experimental data and Fluent solution. On the other hand, Abid's model cannot capture the shock well and predicts the location of the shock wrong. The same comment can be made by analyzing the Mach number contour plot Abid's model.

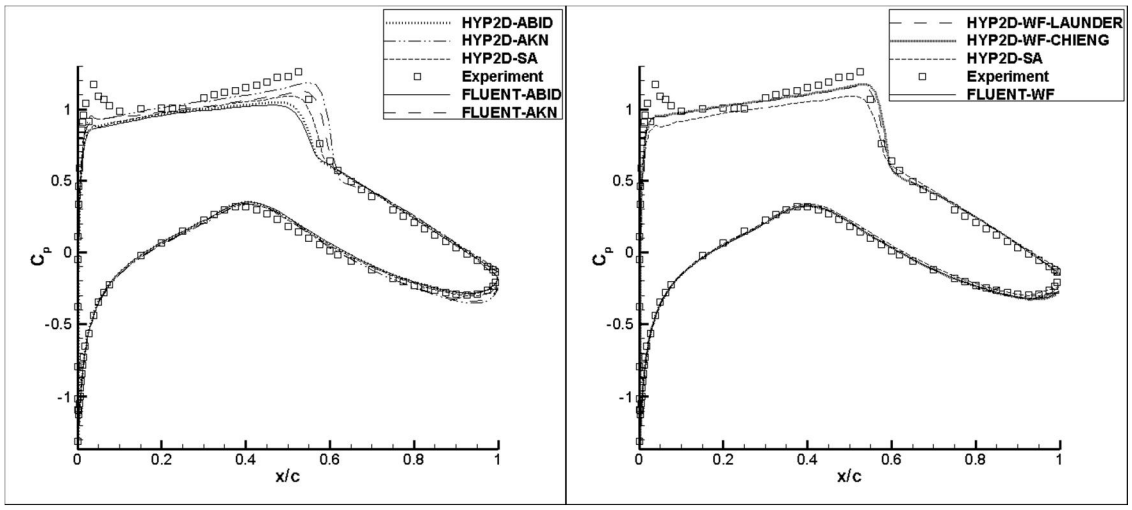

Figure 5.22. Pressure Coefficient Distribution over RAE 2822

In Figure 5.23, the skin friction coefficients on the upper surface of the airfoil are given comparing with Fluent and experimental data as well as Spalart-Allmaras model. The results show that all models but Abid are in the same trend with the experimental data. However, Abid's model overpredicts the skin friction coefficient. The success of Spalart-Allmaras in predicting the near-wall velocity profile can be seen from the skin friction distribution.

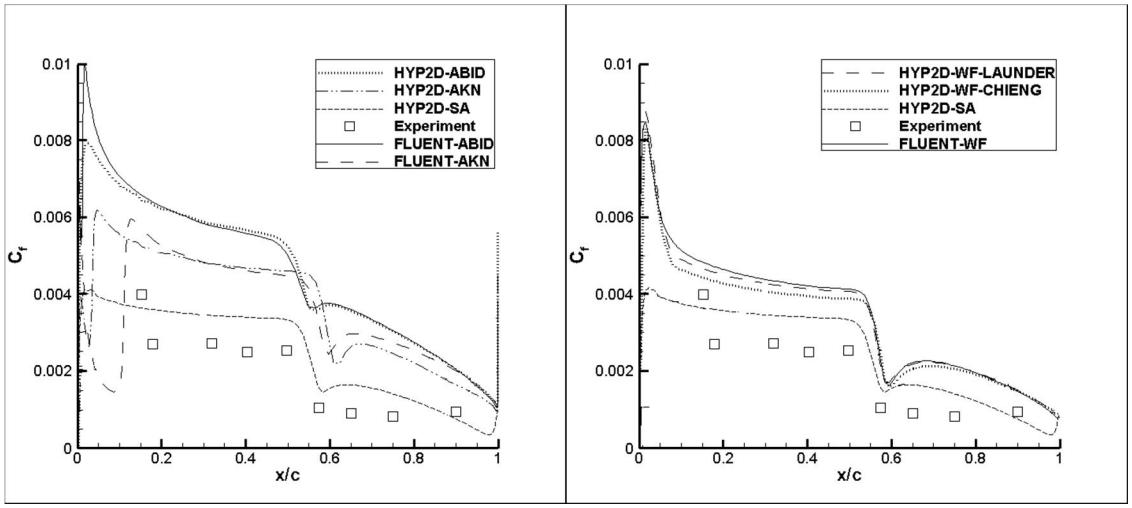

Figure 5.23. Skin Friction Coefficient Distribution at the Upper Surface of RAE 2822

5.2 NACA 0012 Airfoil Application

After validating the several turbulence models, the applications of the models for flow over well-known symmetric airfoil NACA 0012 are performed. Harris from Langley Research Center [31] conducted a series of experiments for different angles of attack at all flow regimes but supersonic in order to determine the pressure distribution over NACA 0012 airfoil. The sketch of the airfoil is given in Figure 5.24.

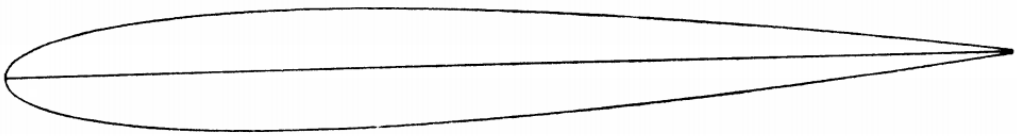

Figure 5.24. Sketch of NACA 0012 Airfoil

In the scope of this thesis, three of the cases reported in [31] and a higher angle of attack case are studied in detailed for which the specifications of the flow are given in Table 5.3.

Table 5.3. Flow Conditions for NACA 0012 Airfoil Simulations

	Case 1	Case 2	Case 3	Case 4
M_∞	0.5	0.5	0.5	0.5
α	1.86°	5.86°	10.86°	12°
Re	9 x 10^6	9 x 10^6	9 x 10^6	9 x 10^6

Although simulations performed for all cases using both wall functions and LRN models, the flow around the airfoil is represented by the results obtain from the simulations conducted using Launder-Spalding wall functions. Mach number distributions around NACA 0012 under given conditions in Table 5.3 are presented in Figure 5.25 and Figure 5.26. It can be seen from the related figures that flow detaches on the upper surface of airfoil at 10.86° and it becomes more definite in 12°. Since

pressure difference between the upper and lower surfaces of the airfoil widens, the lift generation increases up to the stall angle.

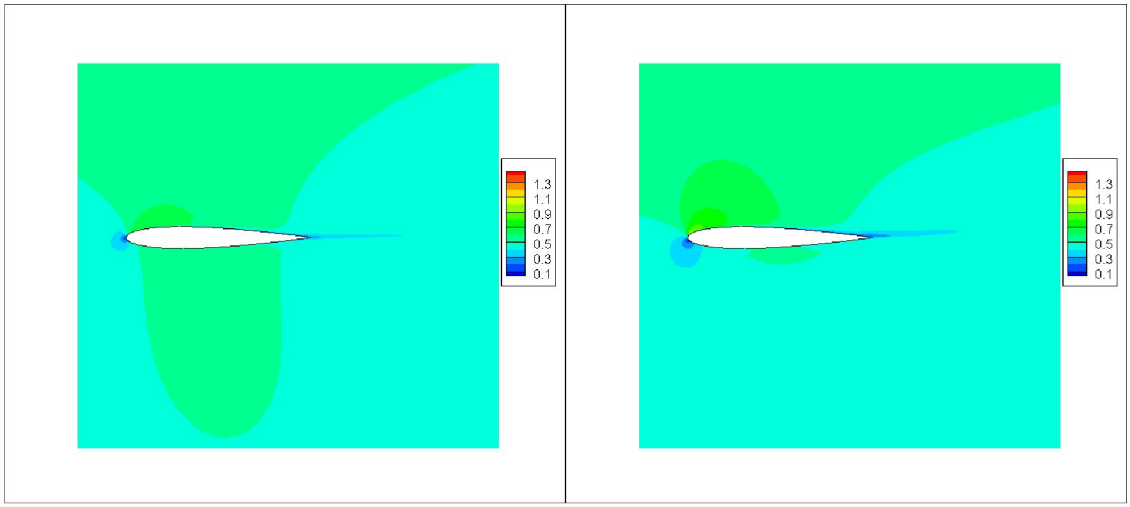

Figure 5.25. Mach Number Contours around NACA 0012 (left: Case 1, right: Case 2)

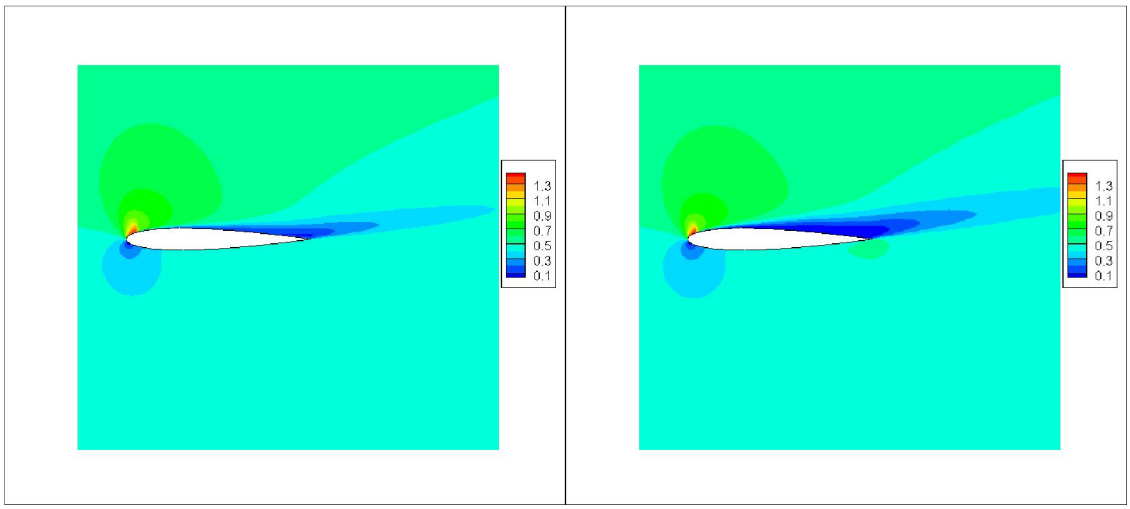

Figure 5.26. Mach Number Contours around NACA 0012 (left: Case 3, right: Case 4)

The turbulence characteristics are presented by turbulence kinetic energy contours for different angle of attacks in Figure 5.27 and Figure 5.28. It can be clearly seen that the generation of turbulence kinetic energy due to velocity gradients on the upper surface of airfoil increases the turbulence kinetic energy directly. In addition, the dissipation rate is also low to destruct this energy at high angle of attacks. Therefore, it is inevitable to face high turbulent effects on the upper surface and wake region.

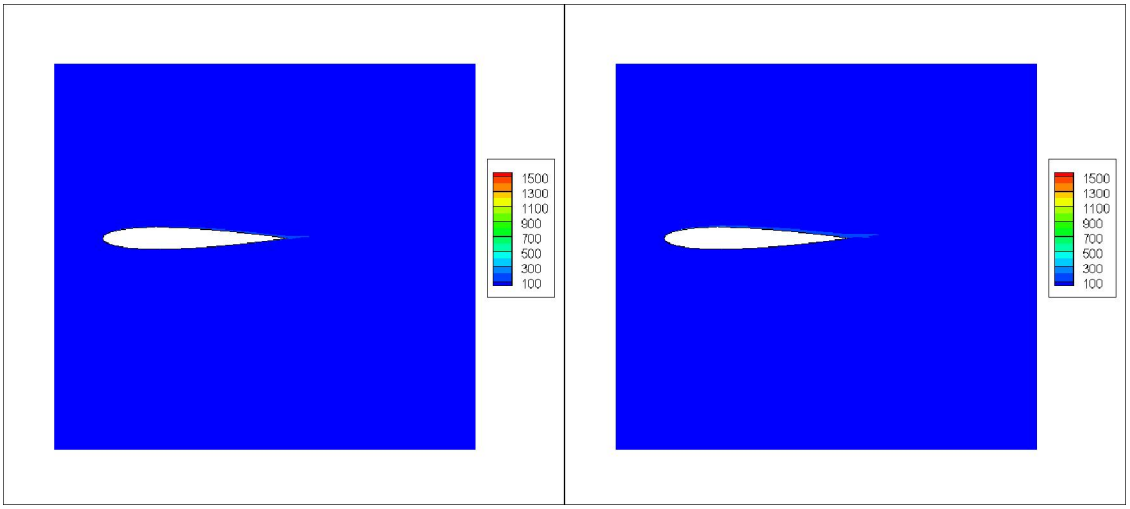

Figure 5.27. Turbulence Kinetic Energy [m^2/s^2] Contours around NACA 0012 (left: Case 1, right: Case 2)

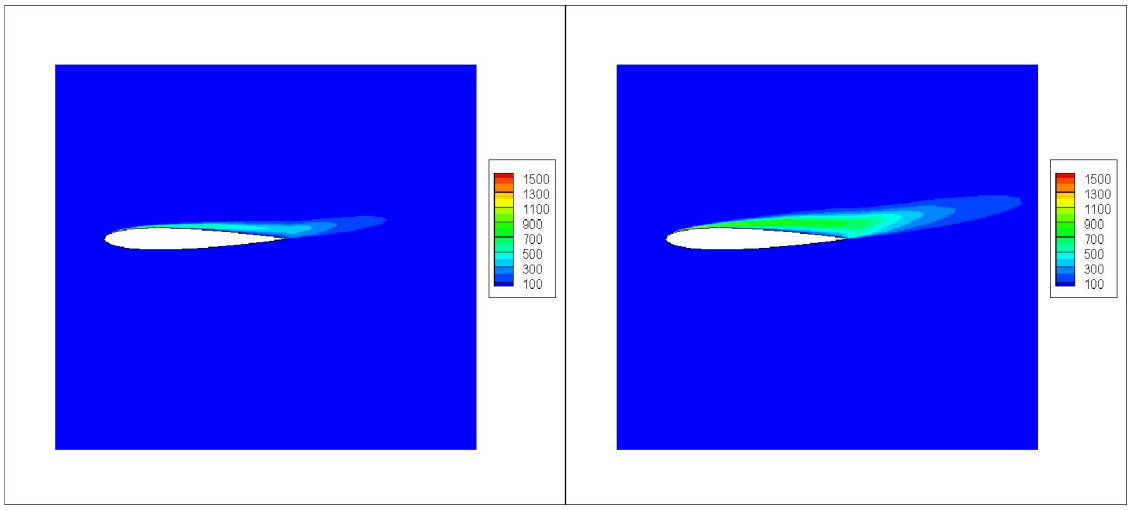

Figure 5.28. Turbulence Kinetic Energy [m^2/s^2] Contours around NACA 0012 (left: Case 3, right: Case 4)

The effect of turbulence on the fluid motion can be summarized by representing the amount of turbulent viscosity. In Figure 5.29 and Figure 5.30, viscosity effects due to turbulence on the flow are given by means of turbulent viscosity contour plots. At low angle of attacks the turbulence becomes relatively unimportant around the airfoil, although it is quite important in boundary layers. Because of high energy of eddies over the airfoil, viscosity generated by the turbulent eddies affects the diffusion of flow parameters highly in the high angle of attack cases. This phenomenon can be seen in Figure 5.30. The turbulent viscosity near of the trailing edge increases up to 1000 times of molecular viscosity of air for Case 4. Therefore, it is very important to include the effects of turbulence for such cases.

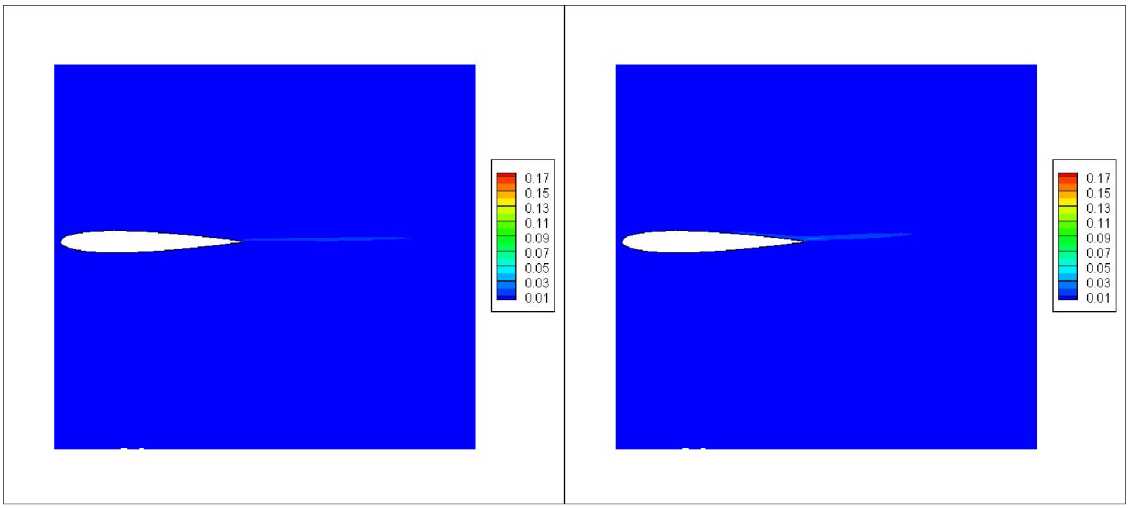

Figure 5.29. Turbulent Viscosity [kg/m s] Contours around NACA 0012 (left: Case1, right: Case 2)

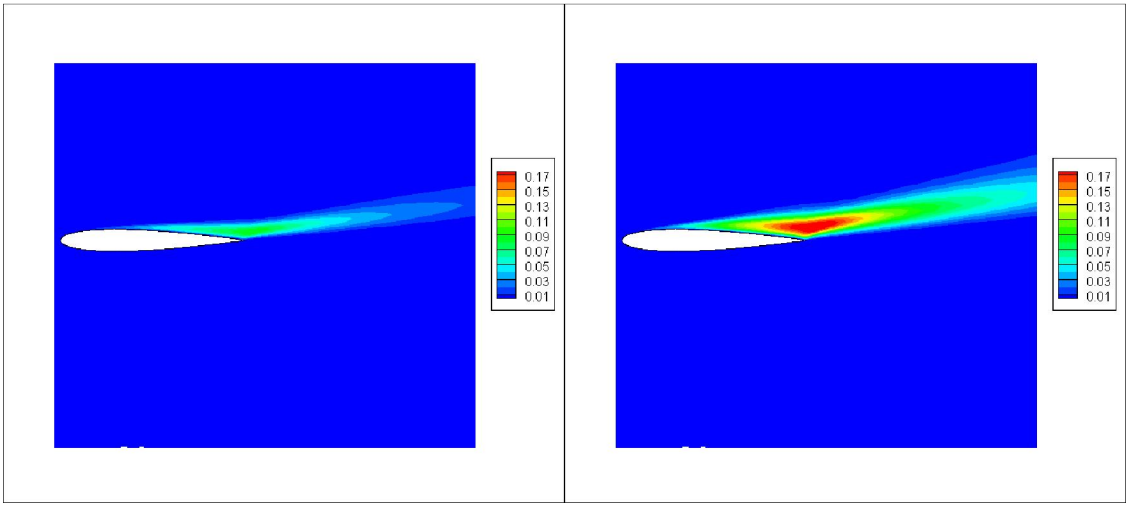

Figure 5.30. Turbulent Viscosity [kg/m s] Contours around NACA 0012 (left: Case3, right: Case 4)

The aerodynamic coefficients with respect to angle of attack obtained from simulations are submitted in Figure 5.31. The models exhibit the same trends for lift coefficient for low angle of attacks. Between 10.86° and 12° wall functions predict a stall-like

characteristic while LRN models do not. The predictions of drag coefficients are consistent for LRN models and wall functions although there is a small discrepancy.

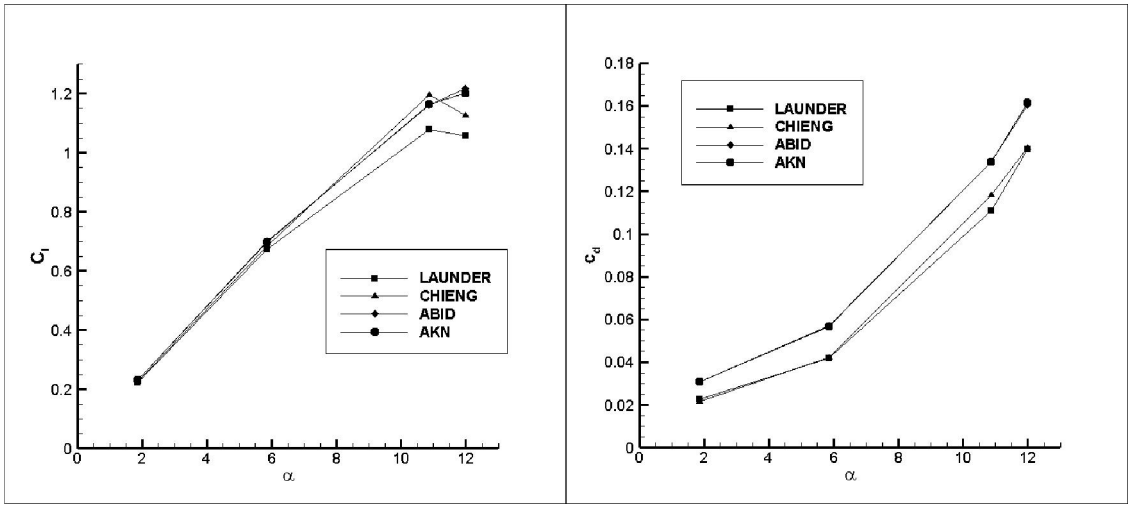

Figure 5.31: Lift and Drag Coefficients with respect to Angle of Attack for NACA 0012

Given the turbulent flow field and aerodynamic loads around NACA 0012 at different angle of attacks, pressure coefficient distributions obtained from LRN models and wall functions are compared with the data gathered from the works of Harris [31] in Figure 5.32. Since there is no data available for Case 4, comparison of pressure coefficient distribution for this case is not performed. All models yield similar results with each other and experimental data. For Case 3, all models gives a little higher pressure distribution than the experiments.

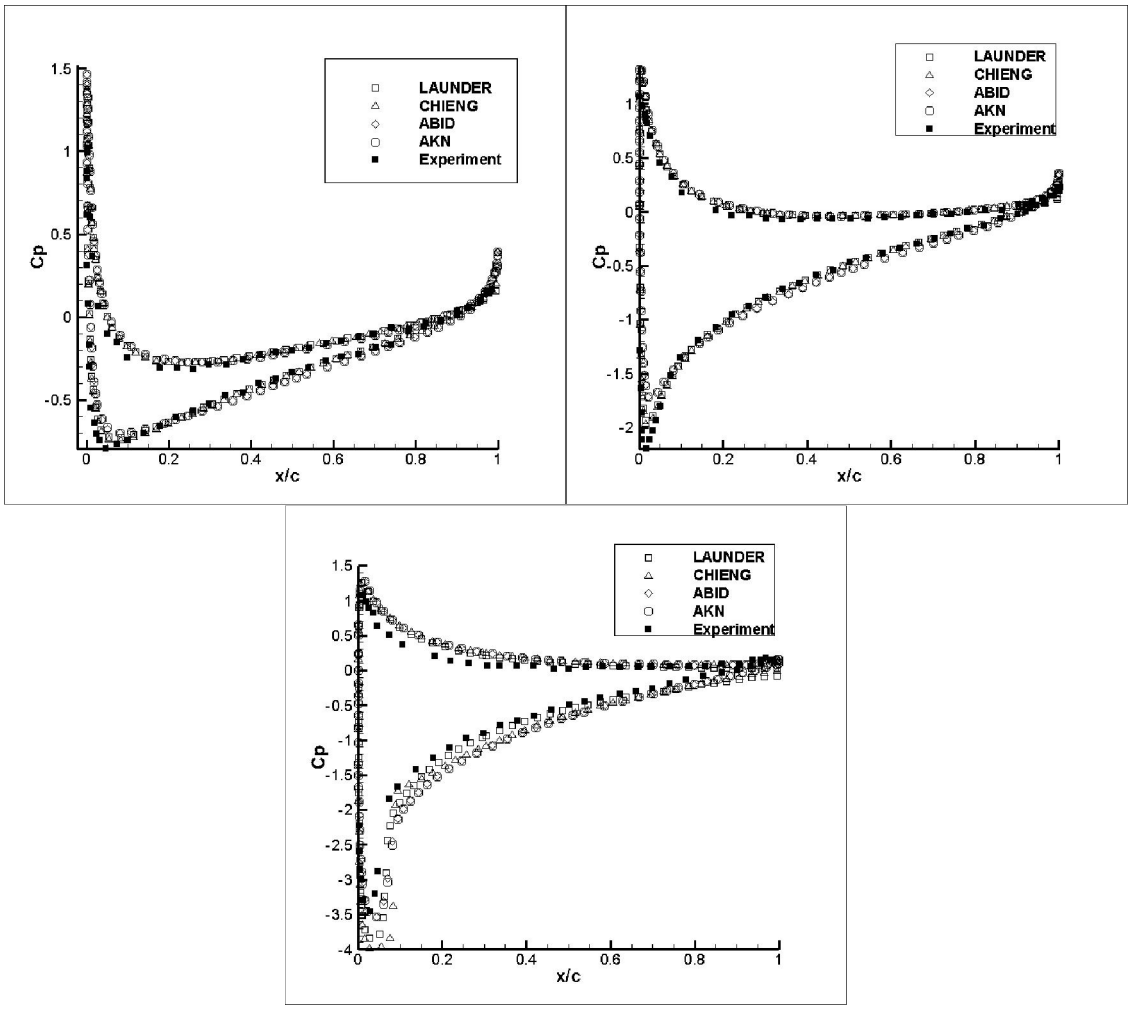

Figure 5.32. Pressure Coefficient Distribution over NACA 0012 (top left: Case 1, top right: Case 2, bottom: Case 3)

In order to assess the parallel performance of the code, the several simulations are performed using different number of processors. CPU time of the solutions are given in Table 5.4.

Table 5.4. CPU Times on Parallel Computations

Number of Processors	CPU Time (sec)
1	8163
2	4155
4	2735
8	1499
16	1317
32	1122

The performance of parallel computations are compared in terms of parallel speedup and parallel efficiency. Speedup, S_n, is defined as the ratio of CPU time spent on serial computation and parallel computation.

$$S_n = \frac{T_1}{T_n} \tag{5.2.1}$$

Here, T_1 represents the CPU time on serial computation where T_n is the CPU time on n processors. The parallel speedup performance of HYP2D is plotted in Figure 5.33. It can clearly be seen that, after 8-processor run the speedup performance of the code is far from the ideal case. For such 2-dimensional grids, parallelization is limited in terms of speedup performance. Parallel efficiency of HYP2D is determined using the following definition of efficiency:

$$\eta_n = \frac{T_1}{T_n * n} = \frac{S_n}{n} \tag{5.2.2}$$

Parallel efficiency of HYP2D for different number of processors is given in Figure 5.34. The efficiency of the code decreases drastically for the parallel solutions using

processors more than 8. Therefore, it can be stated that the most efficient solutions for 2D hybrid grids is obtained using 8 processors for HYP2D solver. It is obvious that more number of processors is likely to yield more efficient computing for 3D cases.

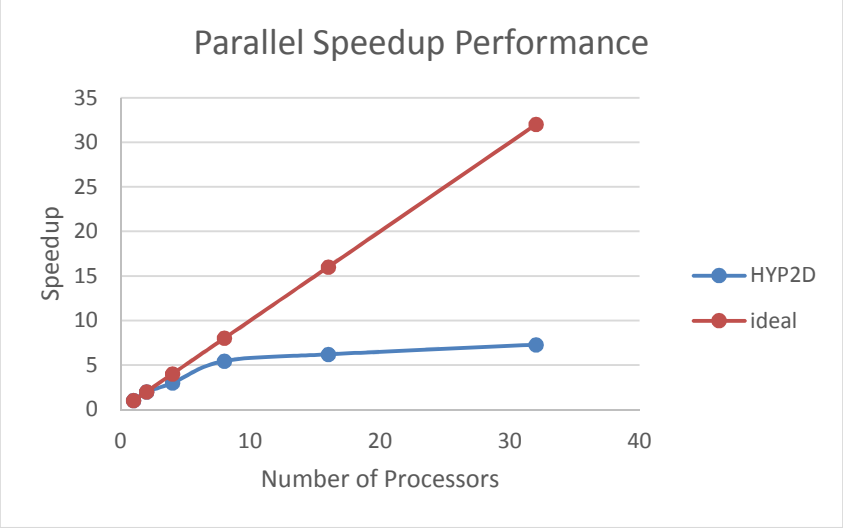

Figure 5.33. Parallel Speedup Performance of HYP2D

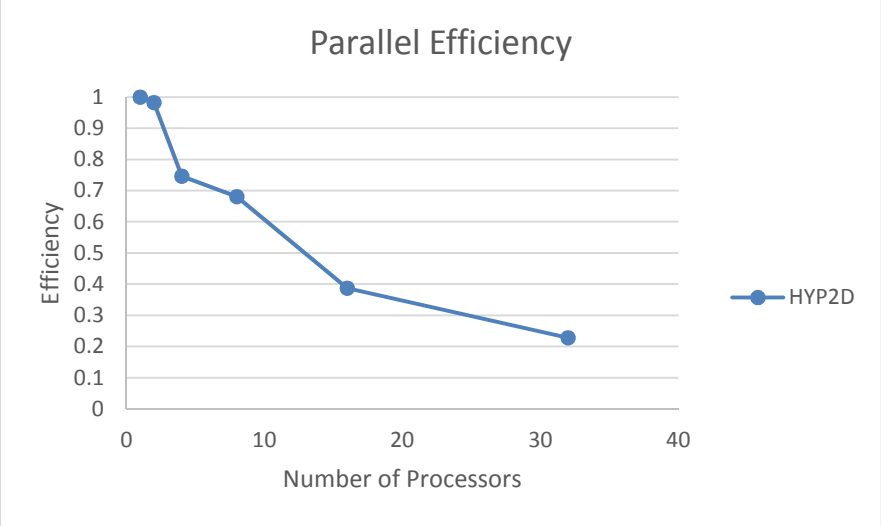

Figure 5.34. Parallel Efficiency of HYP2D

CHAPTER 6

CONCLUSIONS

In this study, the implementation of k-ε turbulence model to a parallel, two-dimensional explicit, collocated, density-based finite volume solver developed for hybrid grids (HYP2D) is performed. In the scope of this thesis, near wall modeling of the turbulence is achieved by applying the wall functions proposed by Launder-Spalding and Chieng-Launder and low-Reynolds-number models of Abid and Abe-Kondoh-Nagano. Validation of the implementation is performed by simulating the turbulent flow over a flat plate and the flow over RAE 2822 transonic airfoil. After accomplishing the validation successfully, an application to simulate the flow over NACA 0012 is performed and results are presented.

For incompressible free stream conditions the velocity profile in the boundary layer over the flat plate are compared with law-of-the-wall theory and results obtained from Fluent software. Skin friction coefficient over the flat plate is also compared by the theoretical values and Fluent results. All comparisons yield good agreement with references. Applying a high subsonic free stream condition to simulate the flow over RAE 2822 computations are performed and turbulent flow fields are compared with Fluent by means of contour plots and consistency is achieved for all models. The velocity profile comparisons show the similar plots before the shock formation. After the shock, LRN models performed better than wall functions in predicting the velocity profile. In addition, pressure coefficient and skin friction coefficients are compared and all models but Abid's LRN model yield similar results. Abid's model shows difficulties in capturing and predicting the shock location. Comparison of k-ε turbulence models with Spalart-Allmaras model points out that Spalart-Allmaras model is more successful in predicting the near-wall region shear stress.

The application of the turbulence models, after successful validation, is conducted on NACA 0012 symmetric airfoil. Four near-wall treatment models are applied for four different angle of attacks 1.86°, 5.86°, 10.86° and 12°. The turbulent flow field is represented and effects of turbulent quantities on mean flow are discussed. In addition, aerodynamic coefficients at different angle of attacks and pressure distribution are submitted and discussed. The prediction of stall angle of LRN models and wall functions shows disagreement. The parallel performance of HYP2D solver is also demonstrated in terms of speedup and efficiency.

6.1 Future Works

For this study;

- Modification of the wall functions with more physical assumptions
- Implementation of other eddy viscosity models and comparison with k-ε turbulence model
- Application of the k-ε turbulence model on 3-D grids

will be the future work for more research.

REFERENCES

[1] Goldstein, S., *Fluid Mechanics in the First Half of this Century*, Annual Review of Fluid Mechanics, vol. 1, p.23, 1969.

[2] Goldstein, S., *Modern Developments in Fluid Dynamics vol. 2*, Oxford University Press, NY, p.331, 1938.

[3] Hinze, J. O., *Turbulence: An Introduction to its Mechanism and Theory,* McGraw-Hill inc., 1959.

[4] Tennekes, H., Lumley, J. L., *A First Course in Turbulence*, the MIT Press, 1972.

[5] Çıray, C., *Akışkanlar Mekaniğine Giriş-Türbülans ve Bazı Türbülanslı Akımlar (Mühendislik Yaklaşımı)*, ODTÜ Yayıncılık, 2013.

[6] Boussinesq, J., *Essai sur la Théorie des eaux Courantes:Mémoires Présentés par Divers Savants à l'Académie des Sciences*, 23, p.46, 1877.

[7] Taylor, G. I., *Trans. Roy. Soc. London. Ser*., A.215., p.1-26, 1915.

[8] Prandtl, L., *Natuwissenschaften*, 13, p.93-108, 1925.

[9] Smagorinsky, J, *General Circulation Experiments with the Primitive Equations, i. the Basic Experiment*, Monthly Weather Review, 91, p. 99-164, 1963.

[10] Smith, A.M.O, Cebeci, T., *Numerical Solution of the Turbulent Boundary Layer Equations*, Douglas Aircraft Division Report DAC 33735, 1967.

[11] Baldwin, B. S. and Lomax, H., *Thin Layer Approximation and Algebraic Model for Separated Turbulent Flows*, AIAA Paper 78-257, 1978.

[12] Bradshaw, P., Ferriss, D. H., Atwell, N. P., *Calculation of Boundary-Layer Development Using the Turbulent Energy Equation*, J. Fluid Mech., 28, p.593-616, 1967.

[13] Baldwin, B.S., Barth, T.J., *A One-Equation Turbulence Transport Model for High Reynolds Number Wall-Bounded Flows*, NASA TM 102847, 1990.

[14] Spalart, P. R., Allmaras, S. R., *A One-Equation Turbulence Model for Aerodynamic Flows*, AIAA Paper 92-0439, 1992.

[15] Kolmogorov, A. N., *Equations of Turbulent Motion of an Incompressible Fluid*, Izv Akad Nauk SSR Ser Phys, 6, Vol 1/2, p.56, 1942.

[16] Jones, W. P., Launder, B. E., *The Prediction of Laminarization with a Two-Equation Model of Turbulence*, International Journal of Heat and Mass Transfer, vol. 15, p. 301-314, 1972.

[17] Launder, B. E., Spalding, D. B., *Lectures in Mathematical Models of Turbulence*, Academic Press, 1972.

[18] ANSYS Inc., www.ansys.com, last visited on December 2013.

[19] Wilcox, D. C., *Turbulence Modeling for CFD*, DCW Industries inc., 1994.

[20] Reynolds, O., *Papers on Mechanical and Physical Subjects*, Vol. 3, The Sub-Mechanics of the Universe, Cambridge University Press, 1903.

[21] Blazek, J., *Computational Fluid Dynamics: Principles and Applications*, Elsevier, 2001.

[22] Versteeg, H.K., Malalasekera, W., *An Introduction to Computational Fluid Dynamics: The Finite Volume Method*, Prentice Hall, 1995.

[23] Reynolds, O., *On the Dynamical Theory of Incompressible Viscous Fluids and the Determination of the Criterion*, Philosophical Transactions of the Royal Society of London. A, v. 186, p. 123-164, 1895.

[24] Chou, P. Y., *On the Velocity Correlations and the Solution of the Equations of Turbulent Fluctuation*, Quart. Appl. Math., vol. 3, p. 38, 1945.

[25] Launder, B. E., Sharma, B. I, *Application of the Energy Dissipation Model of Turbulence to the Calculation of Flow Near a Spinning Disc*, Letters in Heat and Mass Transfer, vol. 1, no. 2, p. 131-138, 1974.

[26] Launder, B.E., Spalding, B., *The Numerical Computation of Turbulent Flows*, Computational Methods in Applied Mechanics and Engineering, 3, p. 269-289, 1974.

[27] Sarkar, S., Hussaini, M. Y., *Computation of the Sound Generated by Isotropic Turbulence*, NASA Contract Report 93-74, NASA Langley Research Center, Hampton, VA. 1993.

[28] Roe, P. L., *Characteristic Based Schemes for the Euler Equations*, Annual Review of Fluid Mechanics, vol. 18, p.337-365, 1986.

[29] Bredberg, J., *On the Wall Boundary Condition for Turbulence Models*, Internal Report 00/4, Department of Thermo and Fluid Dynamics, Chalmers University of Technology, 2000.

[30] Kays, W. M., Crawford, M.E., *Convective Heat and Mass Transfer*, McGraw-Hill Inc., 1993.

[31] Harris, C. D., *Two Dimensional Aerodynamic Characteristics of the NACA 0012 Airfoil in the Langley 8-Foot Transonic Pressure Tunnel*, NASA-TM-81927, 1981.

[32] Ferziger, J. H., Peric, M., *Computational Methods for Fluid Dynamics*, Springer, Third Edition, 2002.

[33] Mavriplis, D. J., Jameson, A., Martinelli, L., *Multigrid Solution of the Navier-Stokes Equations on Triangular Meshes*, AIAA 27th Aerospace Science Meeting, AIAA-89-0120, 1989.

[34] White, F., *Viscous Fluid Flow*, McGraw-Hill, 2005.

[35] Cook, P. H, McDonald, M. A., Firmin, M. C. P., *Aeorofoil RAE 2822 – Pressure Distributions and Boundary Layer and Wake Measurements*, AGARD-AR-138, 1979.

[36] Coakley, T. J., *Numerical Simulation of Viscous Transonic Airfoil Flows*, AIAA 25th Aerospace Science Meeting, AIAA-87-0416, 1987.

[37] Karypis, G.,*METIS-Serial Graph Partitioning and Fill-reducing Matrix Ordering*, http://glaros.dtc.umn.edu/gkhome/views/metis, last visited on June 2014.

[38] Abid,, R., *Evaluation of Two-Equation Turbulence Models for Predicting Transitional Flows*, Int. Journal of Engineering Science, vol.31, no.6, p. 831-840, 1993.

[39] Abe, K., Kondoh, T., Nagano, Y., *A New Turbulence Model for Predicting Fluid Flow and Heat Transfer in Separating and Reattaching Flows-I. Flow Field Calculations,* Int. Journal of Heat Mass Transfer, vol. 37, no.1, p. 139-151, 1994.

[40] Chieng, C.C., Launder, B.E., *On the Calculation of Turbulent Heat Transport Downstream From an Abrupt Pipe Expansion*, Numer. Heat Transfer 3, s. 189–207, 1980.

[41] Craft, T.J., Gant, S. E., Gerasimov, A. V., Iacovides, H., Launder, B. E., *Development and Application of Wall-Function Treatments for Turbulent Forced and Mixed Convection Flows*, Fluid Dynamics Research, 38, p. 127 – 144, 2006

[42] Craft, T.J., Gerasimov, A. V., Iacovides, H., Launder, B. E., *Progress in Generalization of Wall-Function Treatments, Int. Journal of Fluid Flow*, 23, p. 148-160, 2002.